

Numerical and Experimental Simulations of Flapping Wings

Weixing Yuan, Richard Lee, Eric Hoogkamp and Mahmood Khalid

Reprinted from

International Journal of Micro Air Vehicles

Volume 2 · Number 3 · September 2010



Multi-Science Publishing
ISSN 1756-8293

Numerical and Experimental Simulations of Flapping Wings

Weixing Yuan, Richard Lee, Eric Hoogkamp and Mahmood Khalid

Institute for Aerospace Research (IAR), National Research Council (NRC) Canada
Ottawa, Ontario, K1A 0R6, Canada
Weixing.Yuan@nrc-cnrc.gc.ca

ABSTRACT

This paper presents recent progress in a continuing investigation of the aeromechanical aspects of unsteady flapping wings for micro air vehicles (MAV). Numerical simulations were performed for two-dimensional (2D) pitching-plunging airfoils and three-dimensional (3D) flapping wings, mainly at hover conditions, using an in-house code called INSflow. The results were compared with available experimental data obtained in the water tunnel at the NRC-IAR. The investigation revealed that, at hover conditions, the vortices formed during the airfoil plunging motion may remain near the airfoil and affect new vortex formations, and thus the integral aerodynamic performance. In addition, the flow around the 3D insect-like wing is fully three-dimensional. The tip flow affects the flow separation, reducing the separation intensity. Two-dimensional calculations may over-predict the separation and the shedding vortices, thus affecting the generation of aerodynamic forces.

NOMENCLATURE

b	= length of the wing span
$C_D(C_d)$	= drag coefficient based on reference airfoil chord and reference velocity, $C_D = F_x / \frac{1}{2} \rho U_{ref}^2 c b$
$C_L(C_l)$	= lift coefficient based on reference airfoil chord and reference velocity, $C_L = F_y / \frac{1}{2} \rho U_{ref}^2 c b$
C_p	= pressure coefficient, $C_p = (p - p_\infty) / \frac{1}{2} \rho U_{ref}^2$
c	= airfoil chord length
F_x, F_y	= forces in the x- and y-directions
f	= frequency of the flapping motion
H	= plunging amplitude (peak value) of the point about which the airfoil pitches
\bar{H}	= normalized plunging amplitude, $\bar{H} = H / c$
h	= plunging displacement of the point about which airfoil pitches
k_c	= reduced frequency, $k_c = \pi f c / U_\infty$
Re	= Reynolds number based on airfoil chord, $Re = U_{ref} c / (\mu / \rho)$
T	= period of the flapping motion
t	= time
U_{ref}	= reference velocity, $U_{ref} = \ U_\infty + V_{induced}\ $
U_∞	= freestream velocity
u, v, w	= velocity components
$V_{induced}$	= peak velocity of the plunging/flapping motion, $V_{induced} = H\omega$ or $V_{induced} = 0.5b\Gamma\omega$
x, y, z	= Cartesian coordinates
x_0	= pivot location
α	= effective angle of attack at the airfoil leading edge
Φ	= phase difference between pitching and plunging
Γ	= amplitude (peak value) of the root flapping angle
γ	= flapping angle of the leading edge about which the airfoil pitches
λ	= pitch/plunge advanced ratio, $\lambda = \Theta / \tan^{-1}(2\pi f H / U_\infty) = \Theta / \tan^{-1}(2\bar{H}k_c)$
μ	= fluid dynamic viscosity
Θ	= pitching amplitude (peak value)
θ	= pitching displacement (angle) of the airfoil, positive nose-down (tail-up)
ρ	= fluid density

$$\begin{aligned}
 \omega &= \text{angular frequency of the flapping motion, } \omega = 2\pi f \\
 \omega_z &= \text{spanwise vorticity, } \omega_z = \frac{\partial v}{\partial x} - \frac{\partial u}{\partial y} \\
 \bar{\omega}_z &= \text{dimensionless spanwise vorticity, } \bar{\omega}_z = \omega_z c / U_{ref}
 \end{aligned}$$

1. INTRODUCTION

The evolution of a new class of aircraft systems, known as micro-air vehicles (MAV), has been made possible by reliable and fast modelling techniques in aerodynamics and other advances in micro-electronics, sensors, micro-electromechanical systems (MEMS) and micro-manufacturing. Micro-air vehicles are defined as insect-sized aircraft on a five-centimetre scale. Such autonomous flying vehicle research is motivated by a need for intelligent reconnaissance robots capable of discreetly penetrating confined spaces and manoeuvring inside such spaces without direct human interaction.

MAVs require a distinct flight envelope, including hover, perching and flight agility coupled with rapid maneuverability and control at low speeds, which must be achieved with high power efficiency. It does not seem likely that fixed-wing/forward-thrust and rotorcraft (helicopter) designs can completely satisfy the flight envelope specifications for MAVs. On the other hand, insect flight exhibits the required confines of the flight envelope and has been successfully perfected over millions of years of incremental evolution. Insects rely on unsteady aerodynamics brought about by instant adjustments of the wing shape to produce high-lift coefficients and excellent maneuverability. The high lift is a major factor in the increased efficiency of the system. Therefore, engineering realization of the functionality of insect flight is attractive.

Although progress in various enabling technology areas will be required for a practical insect-sized aircraft, the Institute for Aerospace Research of the National Research Council Canada (NRC-IAR), Defence Research and Development Canada – Valcartier (DRDC-V), and Advanced Subsonics Inc., amongst other research institutes, have focused on the efficient generation of propulsive forces through the flapping motion. The dramatic lift-boosting unsteady aerodynamic phenomena that are exploited by insect flapping wings are not yet fully understood. Insect wing kinematics involves non-trivial, instinctive, reciprocal motions. The wing-flapping plane continuously adjusts with the body axis, which also changes rapidly to bring about a certain type of flight. In steady forward flight, the wing flaps in a well-guided fashion to control the leading-edge vortex as it traverses downstream so the horizontal thrust generates the right amount of lift as well as precisely balancing the body drag. Small insects display a variety of hovering motion phenomena. Some small airborne insects hover in an inclined stroke plane where the mean lift coefficient C_L acquired on the downstroke is greater than the maximum possible C_{LMax} of the static condition. This suggests that stall must be present to promote increased circulation required for extra lift. The large downstroke circulation according to Savage et al.¹ and Francis & Cohen² could even be the result of delayed stall of translation. The growth in circulation could even increase its largest value present at C_{LMax} . Such behaviour would be the case in point for birds and bats. A woodpecker maintains a vertical bodyline with wings beating in a horizontal full stroke at very high frequencies. In such hovering motions, the body can be aligned vertically, but the wings must open and close in a “clap and fling”³ manoeuvre so that the large vortex at the opening (fling motion during the downstroke) ends with a small vortex generated at the hinge, which brings about the outer circulation required to provide the precise amount of the lift needed to balance the insect weight. At the end of the upstroke, the leading edges touch and the wings clap together. The wings remain clapped for about 20% of the cycle period, which is believed to correspond to the elastic storage of the high mechanical energy needed for the subsequent fling motion.⁴ The velocity distribution on the wing surface resulting from flapping is non-uniform, creating a complex airflow. It is also unsteady, i.e., the aerodynamic force varies in amplitude and direction during each wingbeat cycle. The variability of the force is compounded by the strong influence of the air viscosity and significant interaction of the wing with its wake, especially in hover. However, our understanding of the resulting aerodynamics is incomplete even on the phenomenological level. Capturing the leading-edge separation is a well-known major obstacle in computational fluid dynamics (CFD) simulations of low-Reynolds-number airfoil flows.

It is clear that a great deal of progress has been made in the past decade towards understanding flapping-wing aerodynamics. Mueller⁵ and Shyy et al.⁶ provide a broader collection and detailed review of previous research work in flapping-wing aerodynamics at low Reynolds numbers. Back in the 1990s, Liu et al. initiated some CFD simulations of hawk moth hovering.^{7,8} As the fluid density is constant in incompressible flow regimes, special treatments are needed to couple the pressure with the velocity for low-Reynolds-number flow simulations. In these simulations, the artificial compressibility

method of Chorin⁹ was used by adding a pseudo-time derivative of pressure to the continuity equation. To model the flapping motion, rotating grids in the entire computational domain were superimposed, which limited the motion pattern when large relative motions between bodies exist. Neef and Hummel¹⁰ performed Euler calculations using the density-based code FLOWer for a NACA 0012 airfoil and a 3D NACA 0012 wing in combined plunging and pitching motions. Since the range of the scheduled motion was appropriately confined, the resulting flow remained essentially attached. Windte et al.¹¹ investigated the laminar flow around a NACA 4402 airfoil at a Reynolds number of $Re = 6000$, again using the Reynolds-averaged Navier-Stokes (RANS) solver FLOWer. At steady onset flow conditions, a significant amount of flow separation occurred over almost the whole range of angle of attack, resulting in a poor recovery of the calculated propulsive efficiencies. This led to a need for a combined plunge-and-pitch motion schedule. For combined motions, the propulsive efficiencies increased notably over a wide range of the resultant thrust. Since the compressible flow equations were employed in Refs. 10 and 11, problems in terms of stability and convergence occurred at low Mach numbers. Thus, a Mach number of 0.3 was used.

With an expressed intent towards an engineering realization of micro air vehicles, it is necessary to develop and validate efficient incompressible CFD tools to obtain deeper insights into the unsteady aerodynamics of simple geometries with large flapping motions. As mentioned above, since the fluid density is constant, a time-independent constraint must be imposed to couple the changes of the velocity field with the pressure field while satisfying the continuity equation. The NRC-IAR is developing an in-house pressure-based CFD code and conducting combined numerical and experimental investigations of these low-Reynolds-number flapping aerodynamics. This paper presents the results obtained during a collaboration with DRDC Valcartier and Advanced Subsonics Inc.

2. DESCRIPTION OF THE IN-HOUSE CFD SOLVER

The in-house code INSflow,¹² developed for computing three-dimensional (3D) unsteady incompressible flows, was applied in this study. INSflow has been used for a number of large-eddy simulation (LES) and unsteady Reynolds-averaged Navier-Stokes (URANS) calculations for various flows in incompressible regimes. Recent numerical investigations of low-Reynolds-number and flapping-wing aerodynamics can be found in Refs. 13-15.

References 13 and 14 present large-eddy simulations of the laminar separation and laminar-turbulent transition of flows past stationary airfoils/wings at Reynolds numbers in transitional regimes. The research work in Ref. 15 attempted the flapping-wing aerodynamics problem by simulating insect-sized airfoils (NACA 0005 and flat plate) in combined large-amplitude pitching and plunging motions. The laminar simulations of the flapping airfoils at a Reynolds number of 3750 showed the leading-edge vortex formation and shedding process. The combination of the pitching and plunging motion simulated in that work resulted in two maximum peaks of the effective angle of attack during each flapping cycle. The simulations showed that the maximum thrust and lift did not occur simultaneously and the occurrence of both the maximum thrust and lift was lagging the (first) maximum peak of the effective angle of attack. When the effective angle of attack passed the first of the two maximum peaks and approached the second, the leading-edge vortex was formed and started shedding through the other half of the motion cycle. The highest thrust occurred when the leading-edge vortex was forming. However, the highest lift was obtained slightly later, i.e., when the effective angle of attack reached the second maximum followed by hysteresis. It appears that the effect of the airfoil's geometry on the averaged lift/drag coefficients is limited. Nevertheless, a thin airfoil seems to be slightly superior to thicker ones, causing less drag and higher thrust coefficients. In addition, the grid resolution affected the vortex shedding prediction and the pitching axis location had a clear influence on the lift and thrust coefficients.

The integral form of the conservation laws of mass and momentum was used in INSflow. A fully implicit second-order temporal differencing scheme was used in the discretization, which made the algorithm stable for large timesteps. The discretization of the convective and diffusive fluxes was carried out in a co-located variable arrangement using a finite-volume approach that was second-order accurate in space. First-order upwind scheme is available. The coupling of the pressure and velocity was handled using the SIMPLE algorithm.¹⁶ The continuity equation was transformed into a pressure-correction equation that had the same general form as the discretized momentum equations. The use of the co-located variable arrangement on non-orthogonal grids required that the SIMPLE algorithm be slightly modified to dampen numerical oscillations. A pressure-velocity coupling method for complex geometries, used by Ferziger and Peric¹⁷, was implemented, where an additional pressure gradient term

was subtracted from the velocity value at the surface of the control volume to prevent non-physical oscillations. A number of two-equation turbulence models and two sub-grid-scale (SGS) models were implemented for Reynolds-averaged Navier-Stokes (RANS) and large-eddy simulations.

The calculations were performed on moving grid configurations. The velocity of the grid movement was included in the governing equations^{12, 18} in an inertial frame of reference. In order to avoid artificial mass sources generated by the grid velocity, a space conservation law was introduced to ensure a fully conservative property in the computations, as applied by Demirdžić and Perić.¹⁹

3. DESCRIPTION OF THE EXPERIMENTAL SETUP

In the past few years, much progress has been made in developing low-Reynolds-number capabilities and technologies at the NRC-IAR. Figure 1 illustrates the NRC-IAR water tunnel. The water tunnel has an open surface test section with a vertical return circuit. The test section is 15 inches wide and 20 inches high. The freestream turbulence level in the tunnel is rated at $u/U_\infty < 1\%$. Much care was exercised in ensuring that the turbulence screens were always free of trapped air bubbles. A preliminary water tunnel experiment was conducted on a 3D insect-like wing performing three degrees-of-freedom (3DOF) motions.²⁰

Figure 2 shows the 2D model two-axis motion system used for this study. Except for the two-dimensional rectangular wing, all of the equipment was above the water surface, including a 2DOF control system and two small one-component strain gauge balances. Since the external balances could measure the vertical forces only, no drag/thrust forces were measured in this study. The airfoil motion (plunging and pitching) was controlled by two vertically parallel rods. The model was well aligned and the pitch angle was accordingly prescribed. Both flow visualization and particle image velocimetry (PIV) measurements are in progress. In this paper, only the lift forces and a sampling of the PIV results are presented for CFD validation purposes. Detailed results of the 2D airfoil measurements will be reported in separate publications.

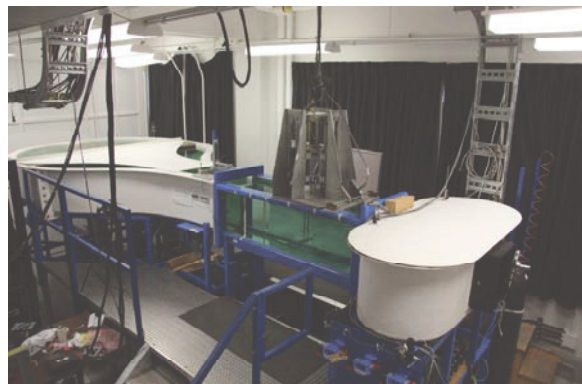


Figure 1. The water tunnel at the NRC-IAR with the two-axis motion system installed.

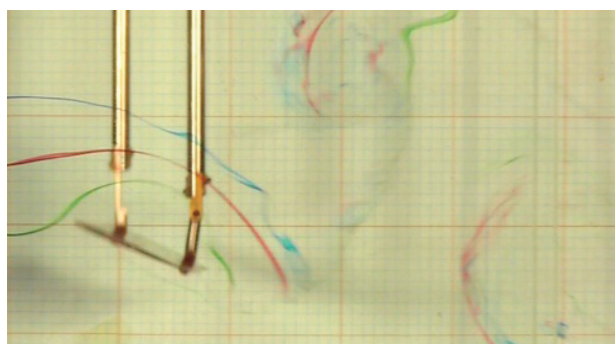


Figure 2. 2D model two-axis motion system.

4. SIMULATIONS OF FLOWS PAST A NACA 0005 AIRFOIL

4.1. Description of Problem and Test Conditions

A symmetrical NACA 0005 airfoil was studied during the collaborative project with DRDC-V and Advanced Subsonics Inc. The airfoil oscillated with combined plunging and pitching motions under a zero or very-low-speed (U_∞) freestream flow condition. The plunging motion of the airfoil was defined as follows:

$$h(t) = H \sin(\omega t + 90^\circ), \quad (1)$$

where H is the plunging amplitude and $\omega = 2\pi f$ is the circular frequency. The pitching motion of the airfoil about the leading edge was described as:

$$\theta(t) = \Theta \sin(\omega t), \quad (2)$$

with a positive angle when pitching counter-clockwise as illustrated in Figure 3 and $\Theta = 30^\circ$.

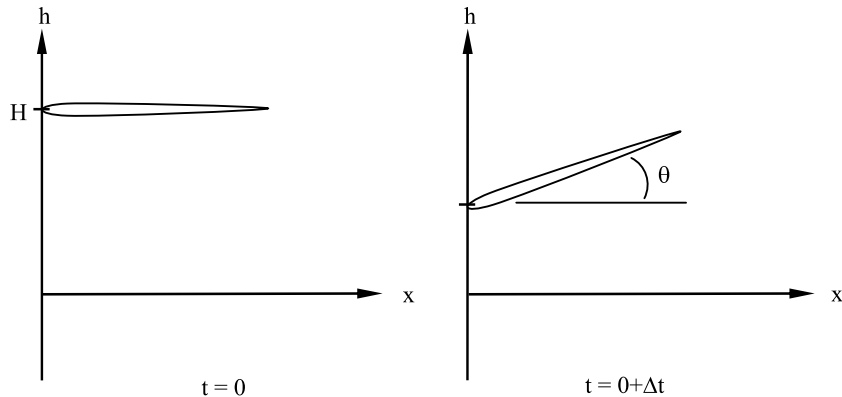


Figure 3. Schematic of the airfoil in plunging and pitching motion.

The airfoil had a chord length of $c = 6.4$ cm. The freestream velocity was specified as $U_\infty = 0.0$ or 0.0635 m/s, to reflect the hover condition. For the latter case, the small freestream velocity was estimated based on disk theory corresponding to the flapping-motion induced velocity, which resulted in a Reynolds number $Re_\infty = \rho U_\infty c / \mu = 4 \times 10^3$. The motion was scheduled such that the plunging amplitude was close to the airfoil chord length ($H = 0.75c$) with a frequency of $f = 0.5$ Hz. The reduced frequency was $k_c = \omega c / 2U_\infty = 1.58$. Identifying the peak velocity of the plunging motion as $V_{induced} = H\omega$, the induced Reynolds number and the reduced frequency could be recovered as $Re_{induced} = \rho V_{induced} c / \mu = 9.7 \times 10^3$ and $k_{induced} = \omega c / 2V_{induced} = 0.67$, respectively. In this study, a generalized Reynolds number based on a combination of these two velocities was used:

$$Re = \frac{\rho \|U_\infty + V_{induced}\| c}{\mu}, \quad (3)$$

which also worked for pure hovering conditions. At the aforementioned flow condition with $U_\infty = 0.0635$ m/s, the generalized Reynolds number was $Re = 10.5 \times 10^3$.

The complex flapping motion will cause a deviation of the local angle of attack from the steady case. For a flapping airfoil in a plunging motion combined with a pitching oscillation about x_0 , at any chordwise location x , the local angle of attack can be expressed as:

$$\alpha(x, t) = -\theta(t) - \tan^{-1} \left[\frac{\dot{h}(t) + \dot{\theta}(t)(x - x_0) \cos(\theta)}{U_\infty + \dot{\theta}(t)(x - x_0) \sin(\theta)} \right], \quad (4)$$

where x_0 indicates the pivot center and understandably takes up a value of $x_0 = 0$ when it is located at the leading edge as considered in this study. In equation (4), the first term in the brackets represents the part of the instantaneous angle of attack at the pivot center induced by the plunging motion, while the second term is the additional change in the local angle of attack induced by the pitching oscillation causing an equivalent cambered wing effect.¹⁵ The derivatives of the motion displacements are as follows:

$$\dot{h}(t) = -H\omega \sin(\omega t), \quad (5)$$

$$\dot{\theta}(t) = \Theta\omega \cos(\omega t). \quad (6)$$

For the values of H , ω and U_∞ used in this paper, the combined motion induced a complex variation of the instantaneous angle of attack at the airfoil leading edge as shown in red in Figure 4. It can be easily verified that the instantaneous flow incidence induced by the plunging motion was much stronger than that from the pitching motion at this selected condition.

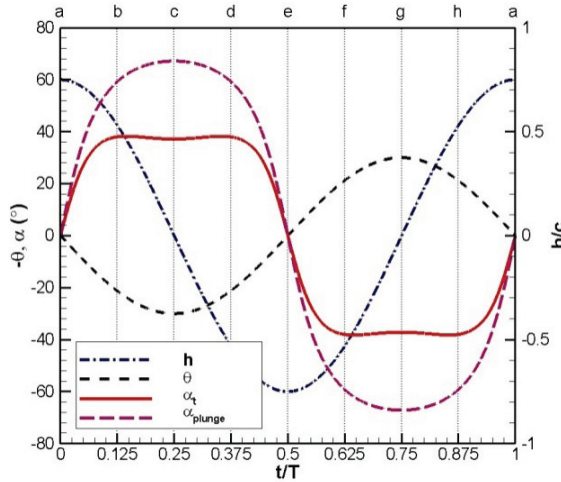


Figure 4. Time history of the effective angle of attack in accordance with the airfoil plunging and pitching motion.

Two-dimensional rectangular wings were used in the water tunnel tests. The wing span was 25.6 cm which resulted in an aspect ratio of 4. End plates were installed to minimize 3D effects. The gap between the wing tips and the end plates was approximately 1 mm, which was close to 0.4% of the span length. The motion control system was carefully validated. The maximum deviations from the described motion schedule were measured to be approximately 0.1° for the maximum pitching angle and 0.1 mm for the maximum plunging displacement, leading to an inaccuracy of the order of 0.4% in pitch and 0.3% in plunge, respectively. The fluctuation of the lift force between successive motion cycles in the experiments reached as much as 30% of the maximum lift.

The 2D calculations were performed on O-type meshes. The farfield boundaries were located at about 25 chords away from the surface of the airfoil. The near-wall domain of the nominal mesh with 481×129 grid points is illustrated in Figure 5. This mesh was designed with a grid density increasing towards the wall at a rate of 6% for the near-wall region and 8.7% for the outer region. The grid lines in the normal-to-the-wall direction were simple straight lines. Improved grid orthogonality would accelerate the calculation convergence and increase the simulation accuracy, but the modification was not investigated in this study. The calculations were started from a stationary fluid. In general, the third cycle produced comparable results to the second cycle for the cases reported in this study.

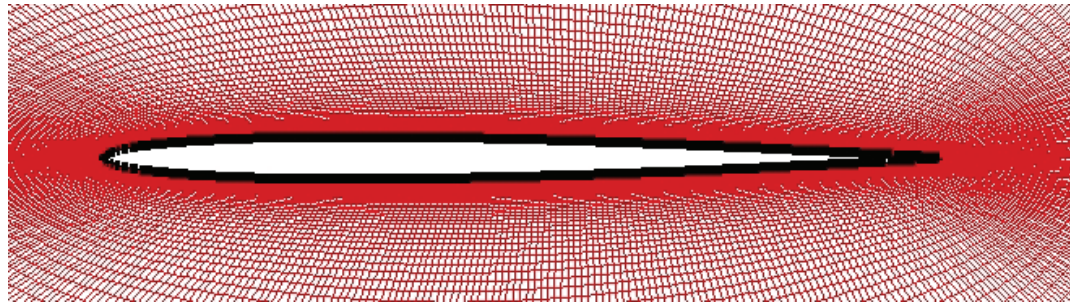


Figure 5. Illustration of the nominal mesh with 481x129 grid points.

4.2. Grid Sensitivity and Numerical Scheme/Timestep Effects Study

Investigations were carried out for the NACA 0005 airfoil. Figure 4 shows the compound instantaneous angle of attack at the airfoil leading edge produced by the combined pitching and plunging motion schedules for the case with $U_\infty = 0.0635$ m/s. Laminar flow was assumed as the Reynolds number was relatively low. To select a suitable grid for the investigations, computations for the case with $U_\infty = 0.0635$ m/s were performed using the second-order spatial discretisation on three O-meshes: 241×97, 481×129 and 961×161, with corresponding timesteps for one plunging cycle of 2888, 3840 and 5760, respectively. Six flapping cycles were conducted for the coarse and medium grids. Figure 6 demonstrates the grid effects on the aerodynamic coefficients. The discrepancies of the results obtained on the coarse and medium grids were minimal. Since the calculations on the fine grid were time consuming, only two cycles were completed; however, two cycles were sufficient for confirmation. Although the discrepancies amongst the meshes were obvious for the first cycle, the aerodynamic coefficients matched well starting from the second cycle. Based on this observation, the results obtained from the medium grid will be discussed in the following sections.

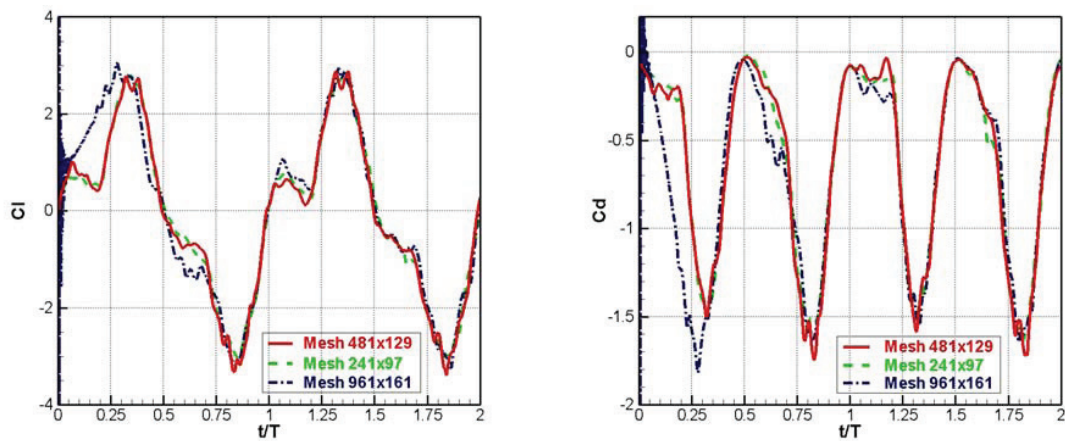


Figure 6. Grid resolution effects on the aerodynamic coefficients of the NACA 0005 airfoil in combined pitching-plunging motion.

Despite the application of varying timesteps to the grid sensitivity study as mentioned previously, another case with an aggressively reduced timestep (one order of magnitude lower, with 384 timesteps per motion cycle) was tested on the 481×129 mesh to clarify explicitly timestep effects. Since first-order schemes are often applied in the simulations of real-world for the specific purpose of suppressing numerical instabilities present in complex problems, indeed towards this end, two further test cases were executed using a first-order upwind scheme. Figure 7 shows the computed results demonstrating the effects of the spatial discretisation scheme and the timestep on the aerodynamic coefficients of the NACA 0005 airfoil. As shown in the figure, the second-order scheme predicted fluctuations while the first-order scheme damped the fluctuations, leading to the development of smooth coefficient curves.

Although the fluctuations obtained using the second-order scheme from the larger timestep did not precisely repeat those from the smaller timestep, the main variation during the course of the motion cycle was the same. Moreover, the results obtained using the first-order scheme from both timesteps overlapped completely. Findings indicate that the timestep for one motion cycle of 3840 is sufficiently small for the present investigation and the other one with 384 divisions combined with first-order scheme is equally appropriate to be applied in the MAV preliminary design.

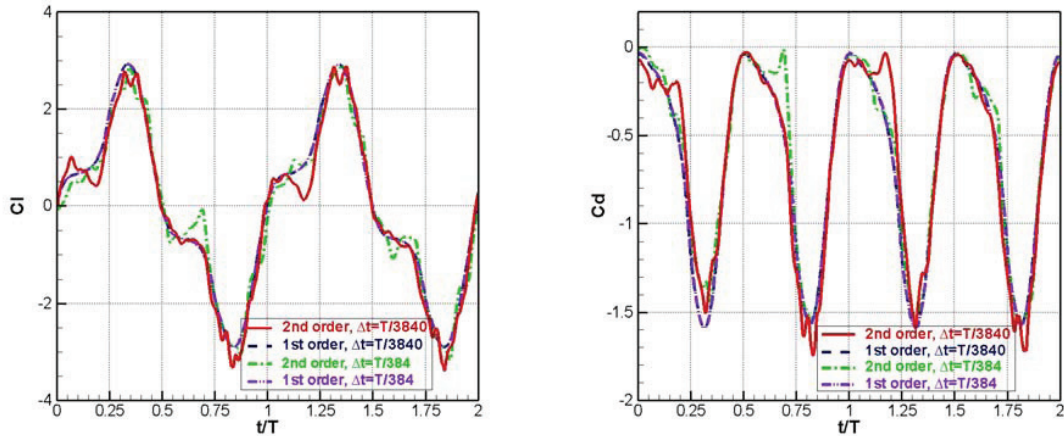


Figure 7. Effects of spatial discretisation scheme and timestep on the aerodynamic coefficients of the NACA 0005 airfoil in combined pitching-plunging motion.

4.3. Lift Coefficients Compared with Experiments

Figure 8 compares the computed lift coefficients of the third and fourth cycles with those obtained in the experiments. In the experiments, about 82 cycles were acquired to avoid influences of the wake circulation, and an ensemble-averaging was carried out. To ensure that the ensemble-averaging was done properly, the first and last few cycles were excluded and then the lift time-series were broken into 24 three-cycle frames. A point-by-point average was taken based on these 24 frames to give an ensemble-averaged three-cycle time-series. While the ensemble-averaged experimental data are presented here, the instantaneous CFD results are depicted since less than six cycles were completed and the CFD results showed less variations from cycle to cycle.

In general, the numerical and experimental results are in good agreement. As the measured data has demonstrated, the lift coefficients displayed repeatable behaviour during the two cycles of the pitch-plunge motion schedule. For $U_\infty = 0.0635$ m/s, the lift coefficients also showed nearly repeatable behaviour (symmetry in time) during the two half-cycles of the pitch-plunge motion schedule, which of course was not the case for $U_\infty = 0$. The latter is believed to be attributed to the flow (vortices) memory effect as discussed later in Section 4.4 on the flowfield analysis. Slight deviations observed between the first and second half-cycles for $U_\infty = 0.0635$ m/s are believed to be related to the flow transition as discussed in the following paragraph, although freestream quality and flow angularity might to certain extent also contribute to these deviations. Particle image velocimetry (PIV) data in support of these observations is currently being processed and will be published in the future for confirmation.

The lift coefficient predicted using the second-order spatial discretisation scheme showed strong variation at the time instants when approaching the neutral center point of the motion ($t/T = 0.25$ and 0.75). At these time instants, the general Reynolds number reached its maximum as a result of the high velocity of the plunging motion. The flow was most probably in a transitional regime. On the other hand, as shown in Figure 4, the plunge-induced angle of attack was near its peak because of the high speed of the plunging motion at these stages. The high effective angle of attack caused a massive flow separation at these time instants, as discussed later. Both flow transition and separation are three-dimensional processes. 3D simulations may help understand and confirm this phenomenon.

Although the freestream velocity $U_\infty = 0.0635$ m/s was low, comparisons of the results between the test cases with and without freestream velocity showed large discrepancies. As shown in the right plot

of Figure 8, the flapping airfoil at zero freestream condition generated higher variations of the lift coefficients. The physics behind such flows will be discussed in the next section.

Furthermore, calculations using a first-order scheme in space were performed as the second-order scheme experienced numerical instabilities in the later 3D flapping-wing calculations. As seen in the figure, the first-order scheme damped the local flow fluctuations to some extent since it introduced higher dissipation. The introduced dissipation was so strong that it smeared the vorticities shed in the wake region at the zero freestream velocity condition, as discussed later. Nevertheless, the first-order calculations predicted major features (magnitude and phase) of the lift coefficient variation at $U_{\infty} = 0.0635$ m/s, which indicates that the first-order scheme can be used for engineering purposes.

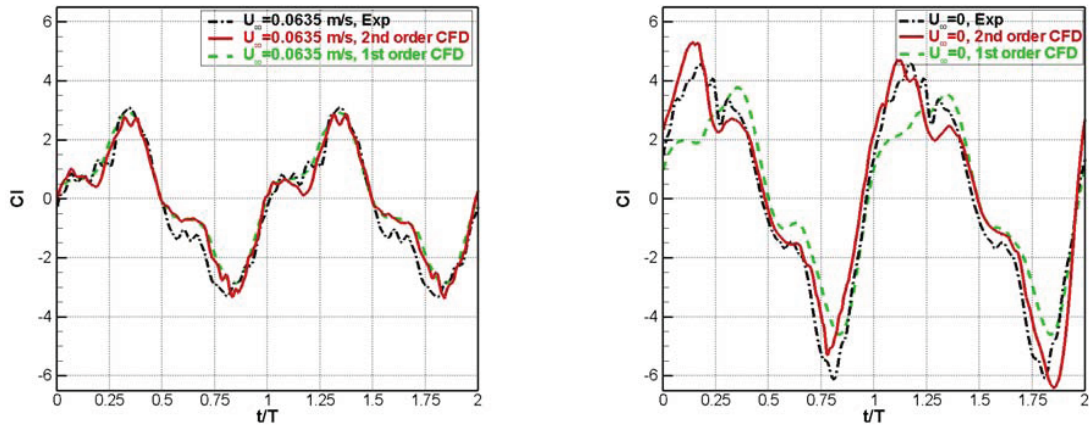


Figure 8. Computed lift coefficients in comparison with experimental results.

4.4. Flowfield over the NACA 0005 Airfoil

The numerical results for the case with $U_{\infty} = 0.0635$ m/s are shown in Figure 9 and Figure 10. Figure 9 shows the computed pressure distributions and streamlines around the pitching-plunging NACA 0005 airfoil. Figure 10 depicts the corresponding distributions of the spanwise vorticities. The top left picture in Figure 9a corresponds to the start of the downstroke movement at the end of the upstroke after the bottom right snapshot of Figure 9h. It is clear that a leading-edge vortex system had already started to form on the lower surface of the airfoil at the ending phase of the upstroke (Figure 9g), giving rise to the appearance of a twin vortex at the underside of the airfoil in Figure 9h, which was further strengthened at the onset of the down beat in Figure 9a. This leading-edge vortex continued to shed (Figure 9b) and was eventually shed into the wake (Figure 9c). It should be noted that even though the time corresponding to Figure 9b had passed the first peak of the instantaneous angle of attack (cf. Figure 4), no vortex had formed on the upper surface owing to the phase delay. By the time the instantaneous angle of attack was midway approaching the second maximum peak in Figure 9c, a new leading-edge pair vortex system had started to form, but on the upper surface of the airfoil (weak blue color). This vortex is clearly confirmed by the clockwise vorticity (blue color) shown in Figure 10c. Similar to the vortex that grew on the lower surface, the vortex on the upper surface, too, gave rise to a second vortex at the leading edge as it traveled downstream before it shed into the wake in Figure 9d. However, the second one disappeared and the first one was sustained and continued shedding downstream (Figure 9e). The subsequent follow-on process during the upstroke period was similar to the downstroke phase, in a time-dependently symmetric manner.

The current research is focused on the hover condition, where generating sufficient thrust is a technical challenge. As mentioned earlier, to reflect the hover condition, the small freestream velocity was estimated based on disk theory corresponding to the flapping-motion induced velocity. To check the influence of the freestream velocity, another test case with zero velocity at the farfield boundary was carried out. In this case, the flow circulated within the computational domain to maintain the mass conservation. The numerical results for the case with $U_{\infty} = 0.0$ are shown in Figure 11 and Figure 12. Although the flapping frequencies were the same and the freestream velocity of the earlier case was small, the flowfields showed a notable difference at these two flow conditions.

For the case of the pure hover condition with $U_{\infty} = 0.0$ m/s, the flowfield was more “chaotic” showing obvious interactions with the vortices remained from earlier time phases, see flowfield of the fourth cycle shown in Figure 11 and Figure 12. Similar to Figure 9, a leading-edge vortex had already formed (Figure 11g) and further strengthened (Figure 11h) on the lower surface of the airfoil at the ending phase of the upstroke. Different from that shown in Figure 9a, this lower-surface leading-edge vortex was larger, but could not be further strengthened on the start of the downstroke (Figure 11a). When the airfoil plunged downwards, this vortex did not shed “downstream” because of the lack of the convective effects from the “freestream” (Figure 11b). Owing to the push of the airfoil plunging movement and the viscous dissipation, the vortex shrank and eventually migrated toward the region ahead of the airfoil leading edge (Figure 11b and c). Similar to Figure 10c and d of the case with $U_{\infty} = 0.0635$ m/s, a clockwise vortex was formed on the upper surface at the leading edge as shown in blue in Figure 12c and d. However, this leading-edge vortex was too weak to be identified in Figure 11c using the current color scale of the pressure distribution. This vortex was further shed “downstream” on the upper surface during the upstroke period (Figure 12e and f). Unlike the case with $U_{\infty} = 0.0635$ m/s, an additional counterclockwise vortex was observed at the trailing edge (blue in Figure 11b and red in Figure 12b). This vortex became larger because of the suction effects resulting from the airfoil plunging motion (Figure 11b-d). During the upstroke phase, these upper-surface vortices were squeezed by the airfoil movement (Figure 11e-f) and eventually shed into the wake. Nevertheless, these vortices did not disappear, but remained and influenced the flowfield of the next phases, causing a flowfield asymmetric in time. At the end phase of the upstroke, a new leading-edge vortex was formed on the lower surface (Figure 11g). The follow-on process repeated the observations described above.

The calculations were started from a stationary fluid. As the flow topology may be influenced by the initial condition of a given cycle, the flowfield during the upstroke phase did not replicate those of the downstroke stage at zero freestream velocity, cf. the left column vs. the right column in Figure 11 and Figure 12, respectively. It is clear that the trailing-edge separation observed during the downstroke (Figure 11b) did not appear during the corresponding upstroke phase (Figure 11f). The leading-edge separation vortex formed on the lower surface at the ending phase of the upstroke (Figure 11g) did not shed “downstream” but remained in the near region ahead of the leading edge of the airfoil during the downstroke (Figure 11b and c), whereas the leading-edge separation vortex formed on the upper surface at the ending phase of the downstroke (Figure 11 c and d) shed into and remained in the wake during the upstroke (Figure 11e-h). As a result, the asymmetry phenomenon affected the integrated aerodynamic coefficients.

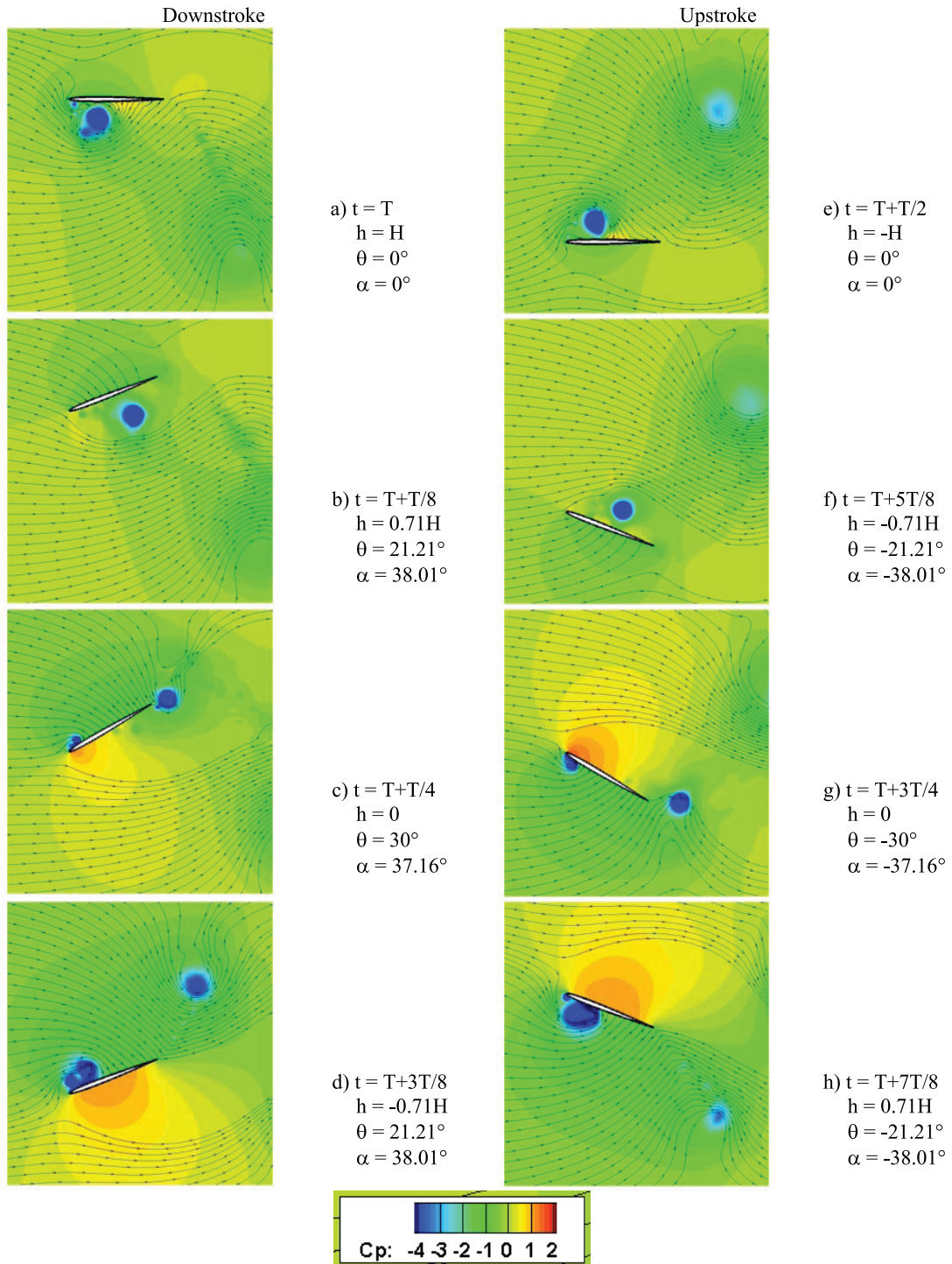


Figure 9. Computed flowfield over the pitching-plunging NACA 0005 airfoil at $Re = 10.5 \times 10^3$, $U_\infty = 0.0635 \text{ m/s}$.

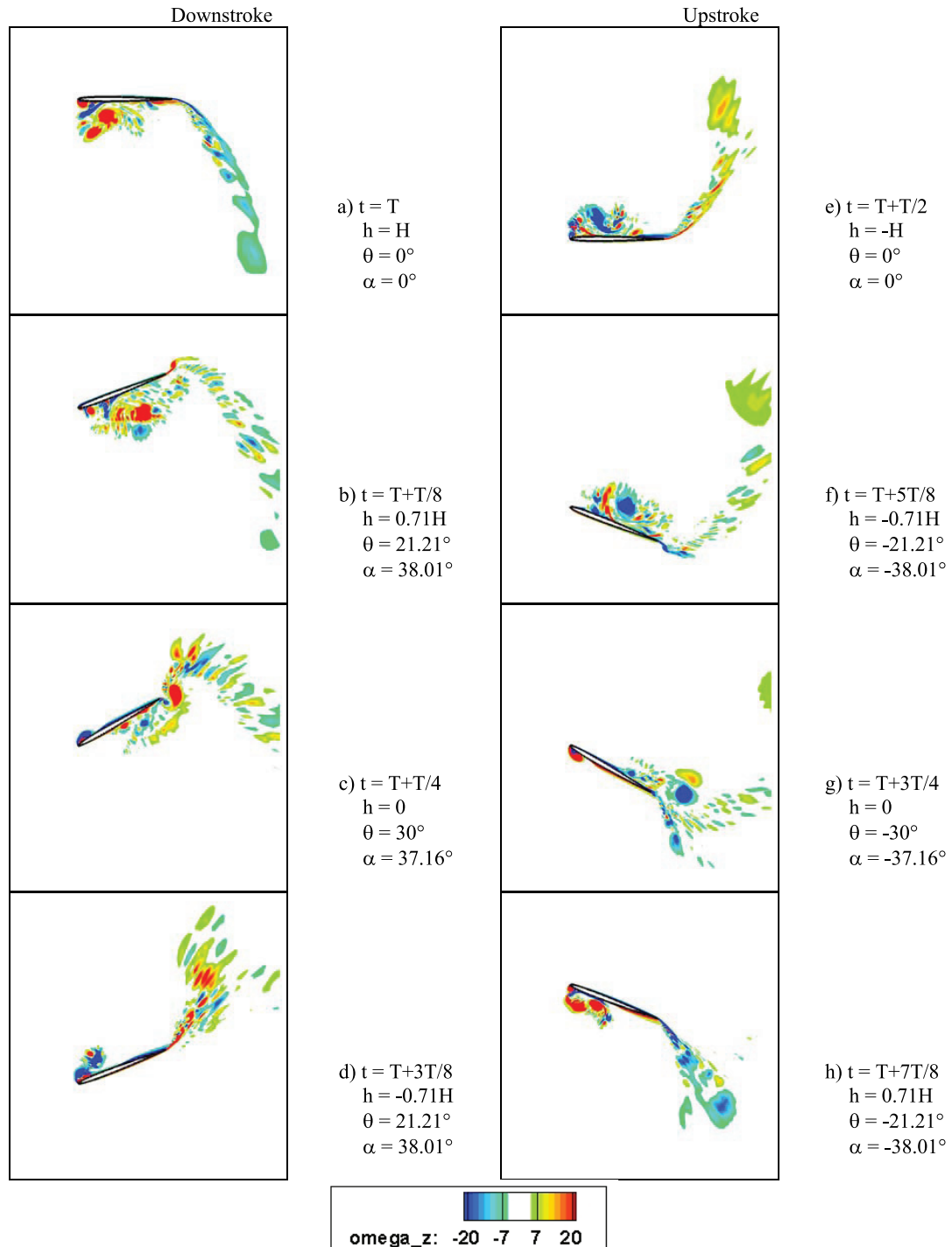


Figure 10. Computed dimensionless spanwise vorticity ($\bar{\omega}_z$) distribution over the pitching-plunging NACA 0005 airfoil at $Re = 10.5 \times 10^3$, $U_\infty = 0.0635$ m/s.

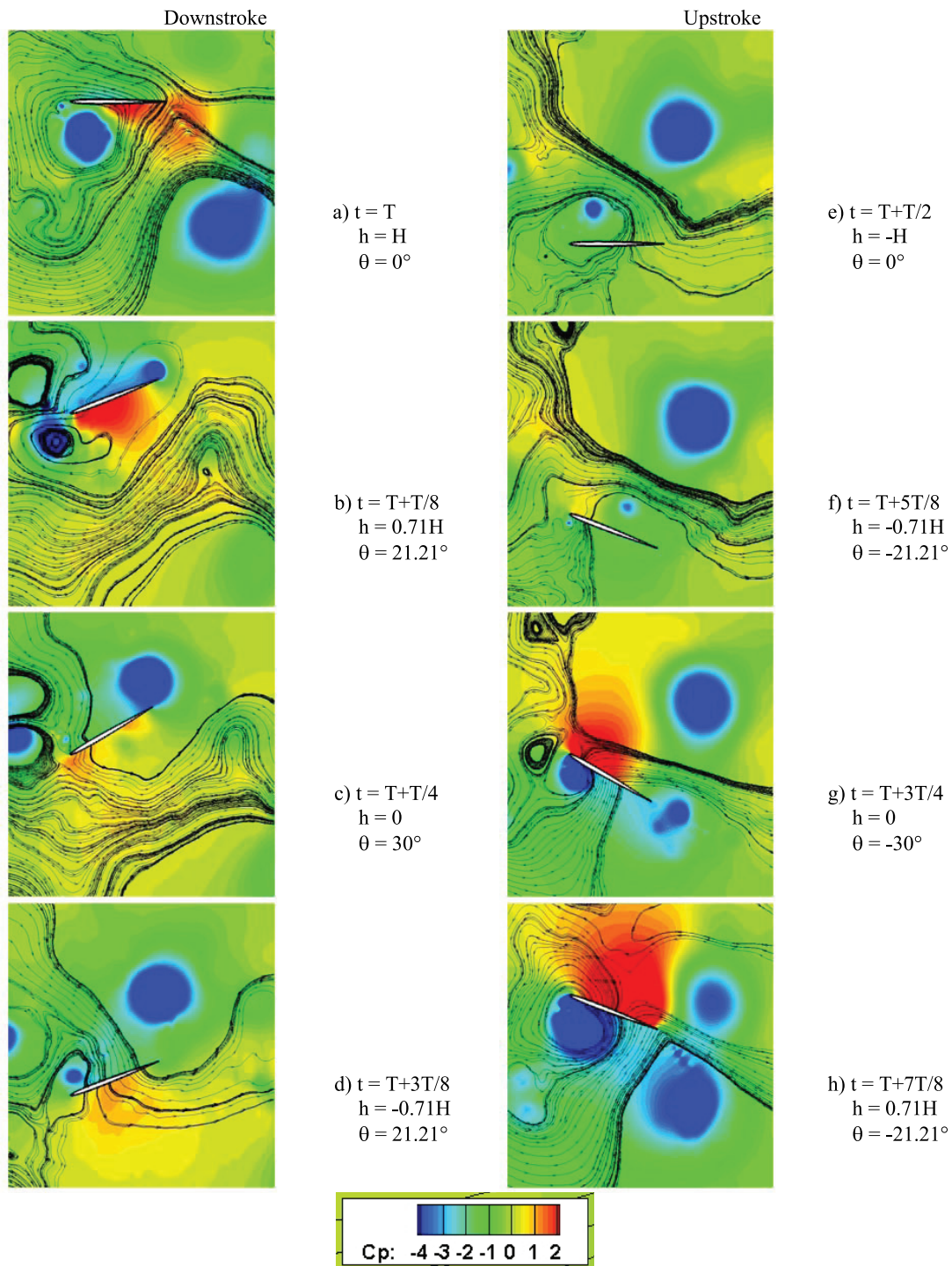


Figure 11. Computed flowfield over the pitching-plunging NACA 0005 airfoil at $Re = 9.7 \times 10^3$, $U_\infty = 0$.

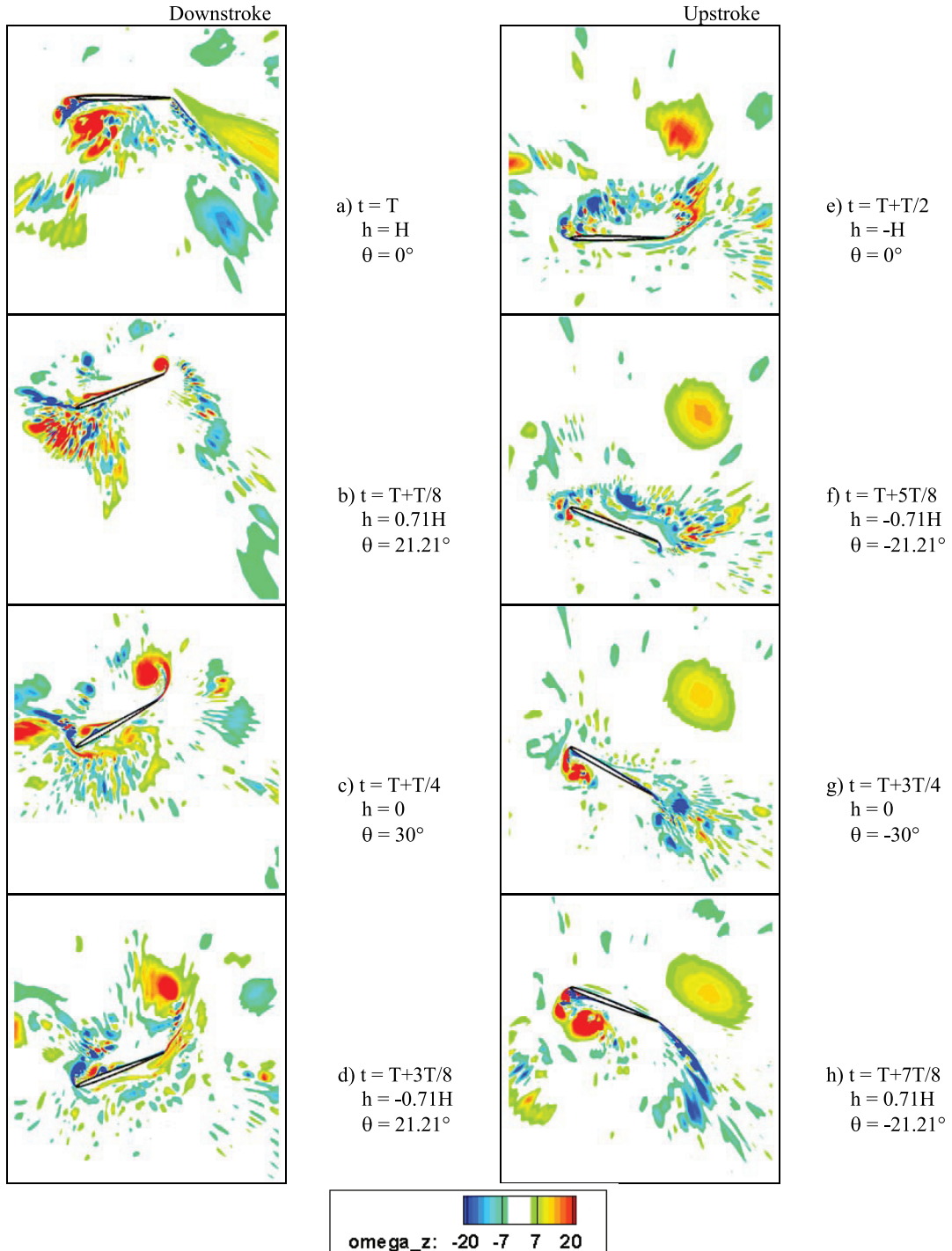


Figure 12. Computed dimensionless spanwise vorticity ($\bar{\omega}_z$) distribution over the pitching-plunging NACA 0005 airfoil at $Re = 9.7 \times 10^3$, $U_\infty = 0$.

Figure 13 shows the resulting aerodynamic coefficients. At $U_\infty = 0.0635$ m/s, the aerodynamic coefficient curves displayed repeatable behaviour nearly symmetric in time during the two half-cycles of the pitching-plunging motion schedule, i.e., both the (positive and negative) peaks of the lift and drag coefficients occurred after $t = 0.25T$ and $t = 0.75T$, respectively. Different from the case with $U_\infty = 0.0635$ m/s, the positive peak of the lift coefficient and the first peak of the thrust at $U_\infty = 0.0$ appeared far before $t = 0.25T$, resulting in an asymmetrical aerodynamic coefficients development in time. The positive peak of the lift corresponded to the “upstream shedding” of the leading-edge vortex from the lower surface of the

airfoil and the formation of the trailing-edge separation as shown in Figure 11b and Figure 11c. It seems that the trailing-edge separation helped the force generation at zero freestream velocity. This time-dependent asymmetry was observed in the experiments as shown in the right column of Figure 8. However, after several cycles of the calculations, the flowfield at zero freestream velocity became more irregular in the calculations with a tendency approaching a distribution symmetric in time as observed at $U_{\infty} = 0.0635$ m/s, while the lift coefficients repeated the time-dependent asymmetry in the experiments. This needs further investigation. It is believed that either the second-order scheme is still too dissipative or the grid is not sufficiently fine to capture accurately the wake vortices and their interactions.

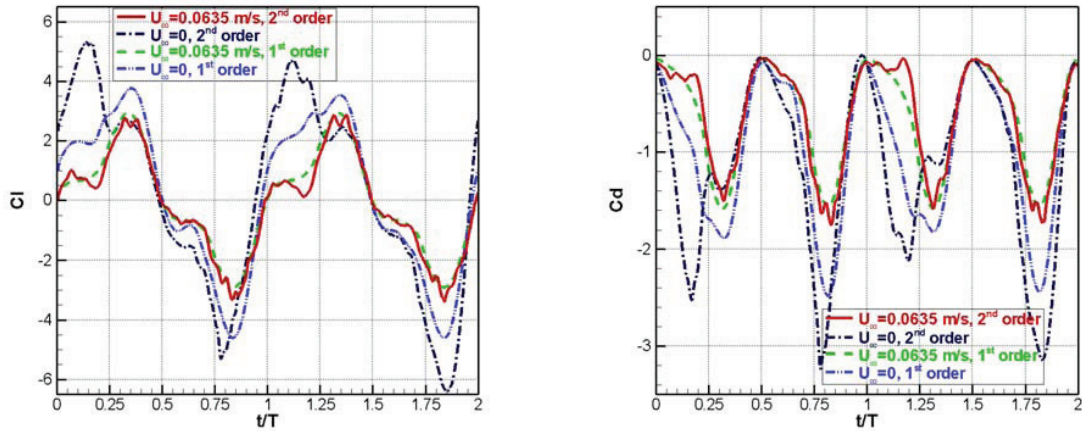


Figure 13. Effects of freestream velocity and numerical scheme on the aerodynamic coefficients of the NACA 0005 in pitching-plunging motion.

It should be noted that, different from the second-order calculations, the computations using the first-order accuracy in space resulted in a flowfield fully symmetrical in time at $U_{\infty} = 0.0635$ m/s and at $U_{\infty} = 0.0$ m/s as shown in Figure 14 and Figure 15. As the first-order scheme was more dissipative, the flowfield was smoother, and some of the flow physics, such as the “fingering” phenomena, observed in the second-order calculations (Figure 10 and Figure 12) were not captured.

It is believed that the fingering, or feathering, features are in fact the signature of individual vortices and their stretching mechanism. Figure 16 illustrates preliminary PIV results which show the spanwise vorticity distribution at two time instants of the pitching-plunging NACA 0005 airfoil. The results were averaged from 24 phase-locked measurements. Individual vortices can be clearly seen. However, whether the vortices were stretched or not must be clarified by the conclusive capture of instantaneous vortices. It is expected that the results averaged from additional phase-locked measurements (say 1000) may be smoother, supporting the first-order CFD prediction shown in Figure 14. It should be noted that large vortices (yellow region in the left plot and green in the right column of the Figure 16) in the wake of the airfoil were leading-edge vortices shed from the previous flapping cycle. They were observed in the second-order CFD simulations but smeared in the first-order numerical calculations.

In addition, the presence of the second primary vortex at the airfoil leading edge was observed in the experiments as appeared as a small red-yellow region in the left plot of Figure 16. The development of this small second primary vortex was observed by Yuan and Khalid numerically.¹⁵ Between the second and the first primary vortices, there was a distinct presence of a counter-rotating region (green in Figure 16). When scrutinizing carefully the CFD results, one can observe that the second primary vortex started to take shape at the conclusion phase of the upstroke, cf. Figure 10g. At this instant in time, the first primary vortex is noticed to have started shedding away from the separated shear layer. Since this vortex was quite intensive and well defined, it gave rise to a counter-rotating region (blue in Figure 10g). The latter is called the secondary vortex. Unlike the first primary vortex, the second primary vortex did not grow in size or intensity owing to the followed downwards pushing of the airfoil movement and eventually disappeared during the downstroke phase, see Figure 10c.

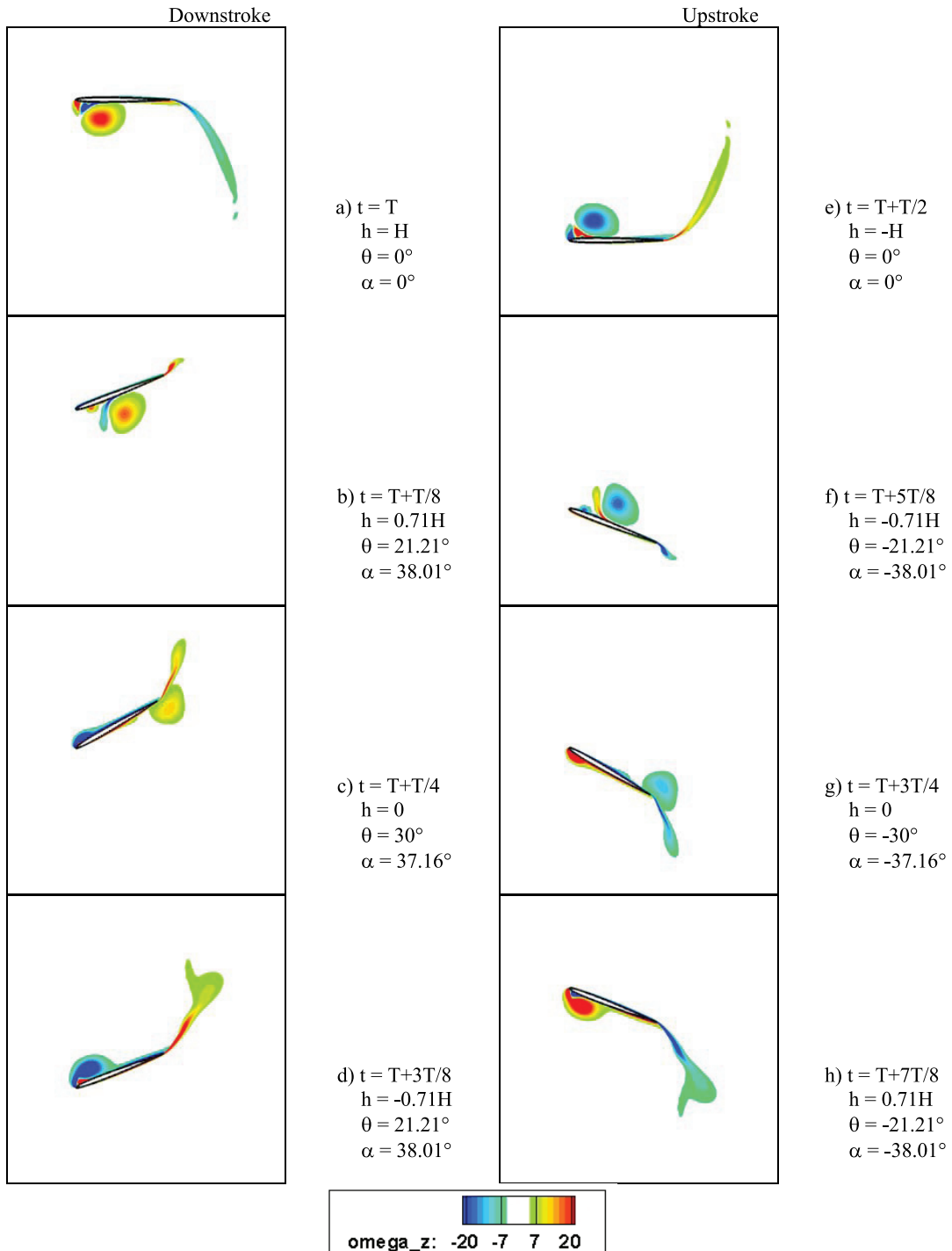


Figure 14. Computed dimensionless spanwise vorticity ($\bar{\omega}_z$) distribution over the pitching-plunging NACA 0005 airfoil at $Re = 10.5 \times 10^3$, $U_\infty = 0.0635$ m/s, first-order CFD.

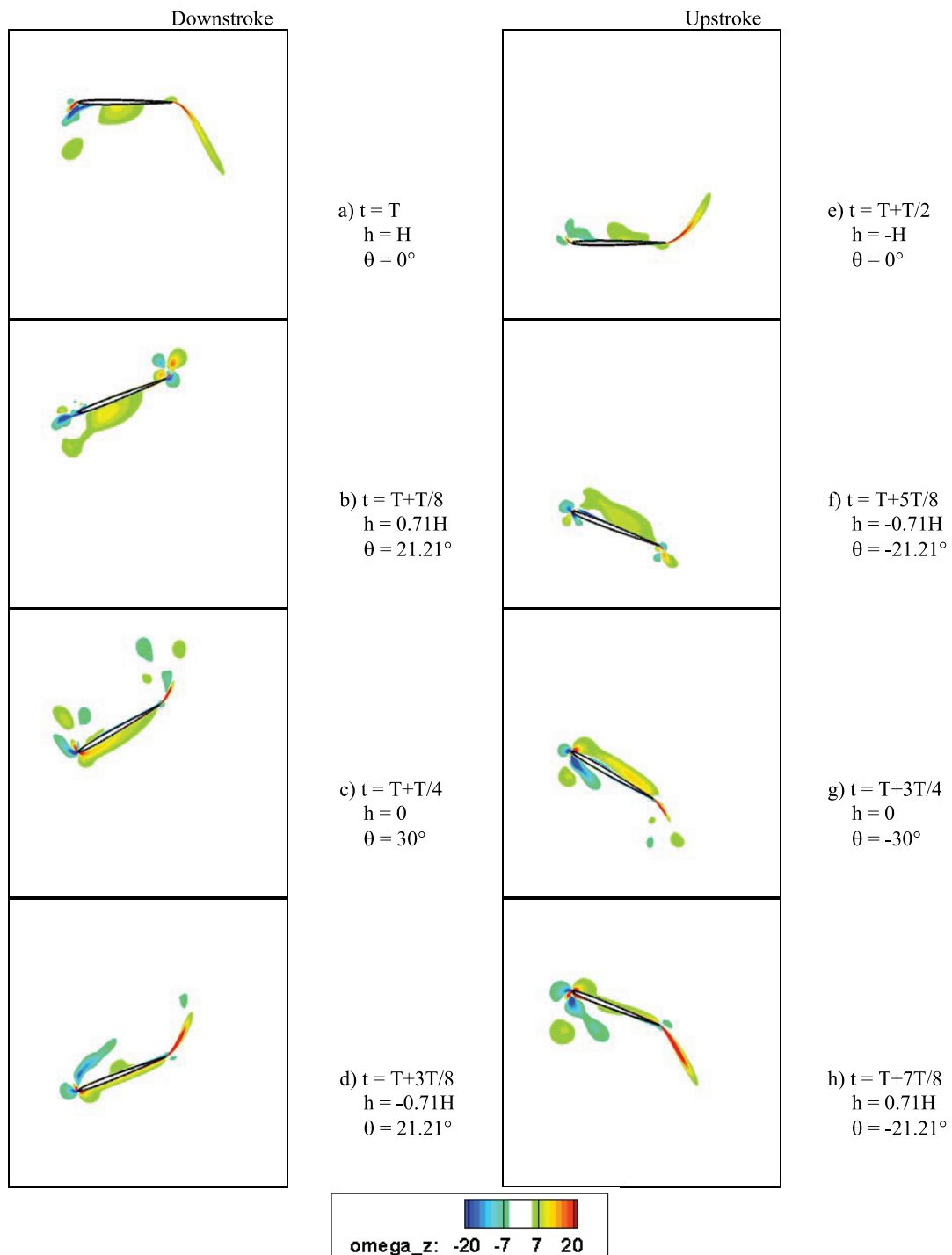


Figure 15. Computed dimensionless spanwise vorticity distribution over the pitching-plunging NACA 0005 airfoil at $Re = 9.7 \times 10^3$, $U_\infty = 0$, first-order CFD.

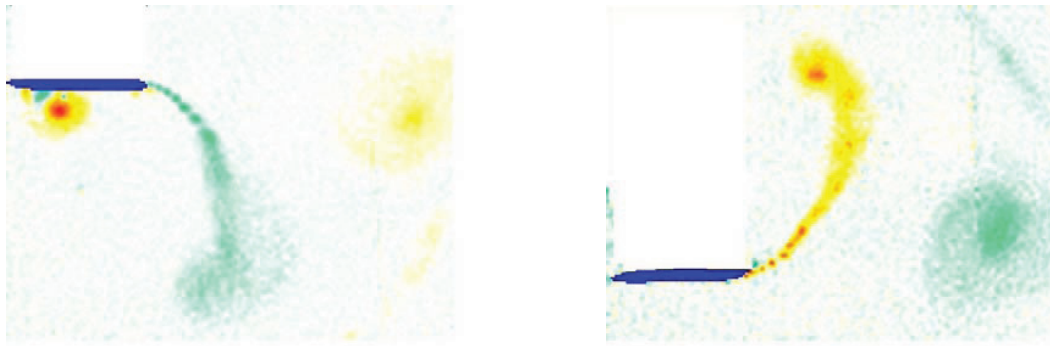


Figure 16. Illustration of the measured spanwise vorticity distribution over the pitching-plunging NACA 0005 airfoil at $Re = 10.5 \times 10^3$, $U_\infty = 0.0635$ m/s, PIV results.

5. SIMULATIONS OF FLOWS PAST 3D INSECT-LIKE WINGS

5.1. Problem Definition

The authors are developing modelling technologies for flapping motions of insect-like wings. A three-dimensional test case was designed by the project team members for experimental measurements in the NRC water tunnel. The 3D test case mimicked closely a future micro-air vehicle. The amplitude to chord ratio of the reference cross-section at 77% of the wing span was assumed to be one. The test case parameters are listed in Table 1. According to Eq. 3, the generalized Reynolds number based on the maximum tip velocity and the reference chord length was 19×10^3 , while it was 15×10^3 based on the maximum velocity at the reference cross-section.

Table 1. Summary of 3D test case variables

frequency	f	0.46 Hz
flap angle amplitude	Γ	15° (0.26 rad)
pitch amplitude	Θ	40° (0.70 rad)
mean pitch	θ_0	0°
phase shift	δ	90° (1.57 rad)
Reference airfoil chord at 77% of wing span	c_{ref}	0.070 m
root chord	c_{root}	0.090 m
tip chord	c_{tip}	0.047 m
freestream velocity	U_∞	0.0635 m/s (2.5 in/s)
kinematic viscosity of the fluid (water)	μ/ρ	1.004×10^{-6} m ² /s
semi span	$b/2$	0.350 m

The wing geometry is shown in Figure 17. The wing planform was slightly different from the wing used by Dickinson and his co-workers in their experiments.^{21, 22} A relatively long wing root extension was needed between the wing root and the flapping axis, owing to the limitation of the installation of a strain-gauge balance, measuring forces and moments in the body axis. Two different airfoils were suggested. One was the NACA 0005 airfoil and the other was a flat plate with a constant thickness of 1/8 inch, which corresponds to approximately 5% thickness. However, priority was given to the symmetrical NACA 0005 airfoil section and its results are reported in this paper.

The 3D motion of the wing was defined as below. The angular displacement of the leading edge of the airfoil due to root flapping was:

$$\gamma(t) = \Gamma \sin(\omega t + 90^\circ). \quad (7)$$

Accordingly, equation (1) represents a two-dimensional version of this motion schedule. The pitching motion of the airfoil about the leading edge was described as:

$$\theta(t) = \Theta \sin(\omega t). \quad (8)$$

The amplitudes of the flapping motion were $\Gamma = 15^\circ$ and $\Theta = 40^\circ$.

The NRC-IAR water tunnel has a 15 in (width) \times 20 in (height) test section as described before. The wing tip clearance distance to the tunnel wall was a function of the combination of the instantaneous flapping and pitching angles. The closest wing tip clearance distance was observed for the trailing edge of the wing tip section, at a position close to the largest flapping angle. It was measured to be 88.4 mm, which corresponded to over 50% of the spanwise dimension of the wing body or nearly two times of the airfoil chord length at the wing tip.

Numerical solutions of the experimental test case are reported here. The experimental test is in progress. Only the preliminary aerodynamic coefficients are presented here and other details will be published elsewhere.

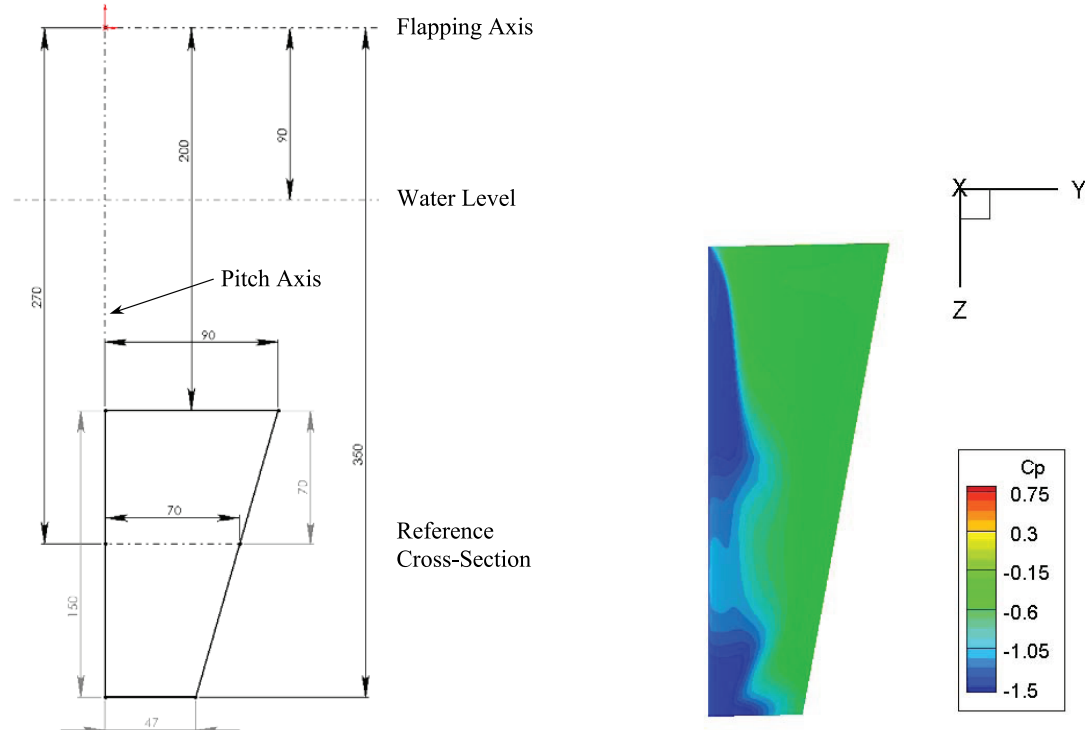


Figure 17. Schematic showing the 3D wing geometry (left, units in mm) and the wind axis system (right).

5.2. 3D Simulation

A grid with $481 \times 129 \times 33$ nodes was used for the flow domain around the wing body, with a farfield boundary located at about 10 airfoil chords. This grid size is comparable to the medium grid used in the earlier 2D calculations, with 33 stations located along the wing span.

The computational domain contained two extensions. The first one stretched from the wing root to the flapping axis, while the second extended beyond the wing tip for 150 mm, which was equal to the spanwise dimension of the wing body. These two extended domains were discretized using grids with $481 \times 133 \times 33$ nodes, thus constituting a three-block structure. Compared with the grid around the wing body, there were 4 extra grid points in the direction normal to the wing surface, to mesh the thickness of the wing root and tip surfaces.

In the calculations, the farfield and the spanwise boundaries were subject to a freestream condition. The calculations were initiated from a stationary state. The computations were found to be time

consuming and no time convergence study was performed. Since the Reynolds number was close to the one in the 2D test case, as many as 384 timesteps per flapping cycle were used to discretize the governing equations in time. An upwind scheme was used for the discretization in space as the second-order scheme encountered numerical instabilities. The computed results are depicted in Figure 18 to Figure 24.

Figure 18 and Figure 19 show the pressure and spanwise vorticity distributions on the reference cross-section (see Figure 17) at different positions in the flapping cycle. It is clear that flow separation at the leading edge was observed most of the time, which is corroborated by the statement of Ruijsink et al.: "small birds and insects are flapping often in a separated flow".²³

It should be noted that the earlier 2D test case was designed to represent closely the main working portion of the flapping wing of a future micro-air vehicle. The reference cross-section was chosen because it was close to the main working portion of the wing. Because of the limitations of the water tunnel rigs, the earlier 2D test case was slightly different from the working condition of the reference cross-section of the 3D flapping wing. To evaluate the adequacy of the representation of the 2D calculations for the reference section, another 2D test case was performed. The 2D test case mimicked the reference cross-section motion of the 3D flapping wing, with the same chord length. Accordingly, the pitching and plunging amplitudes were set to 40° and one chord, respectively. The results of the 2D calculations using the first order scheme as applied in the 3D simulations are shown in Figure 20.

Compared with the 2D case shown in Figure 20, the flow of the 3D flapping wing separated earlier on the upper surface of the reference cross-section, see Figure 18b and Figure 19b, at the time when the airfoil just reached the maximum effective angle of attack. However, on the lower surface, the vortex shed from the primary separation shown in Figure 18a and Figure 19a did not travel far downstream but disappeared in the next snapshots (Figure 18b and Figure 19b). The typical vortex size in the present 3D case was also notably smaller at the local station compared to the vortices observed in the 2D simulations in Figure 20. The reason for quicker dissipation was most probably a result of a three-dimensional interaction, as spanwise effects cannot be reflected in 2D calculations.

Figure 21 and Figure 22 show the flowfield at the sections near the root and the tip of the wing during the first half cycle of the flapping motion. In general, the flow separation at the leading edge was not as extensive as observed at the reference section. At the root, the flapping-induced velocity was smaller than that at the reference cross-section, and therefore, the effective angle of attack was smaller, resulting in mild leading-edge separation. As a result, the flow was not observed to separate at the root at $t = T/4$ as shown in Figure 21b. Although the flow was separated near the tip at this moment (Figure 22b), the leading-edge separation was clearly not as strong as observed at the reference section (Figure 18b and Figure 19b). This is believed to be caused by the tip vortex flow as shown in Figure 23.

Figure 23 shows the flowfield around the wing root and tip at the mid cross-section (y - z plane) in the freestream direction of the flapping wing. Note the presence of a distinct wing-tip vortex as the flow from one surface worked its way towards the other surface and then rolled up as it traveled downstream. During the downstroke period, the wing tip induced flow from the lower surface to the upper surface (Figure 23c and e). The tip flow reduced the flow separation on the upper surface near the tip shown in Figure 22b and c when compared with the flow separation at the mid section shown in Figure 19b and c.

Note that the leading-edge separation was still intensive near the wing tip at the time instant when the wing flapped through the middle position (Figure 22c and d). At these time instants, the wing movement speed induced by the flapping motion was very high causing a high effective angle of attack. The induced tip vortex was not sufficiently strong to smear or eliminate the intensive leading-edge separation.

In terms of the trailing-edge vortex, the extent of the emerging vortex street was noticeably sensitive to the local airfoil section. Its 2D image at the tip was observed to be smaller than its size at the middle or the root sections. Furthermore, it was noted that the slope of the developed wake owing to the flapping induced velocity also increased along the length of the span starting from the root section. This effect is clearly demonstrated towards the right column of Figure 21, the left column of Figure 19 and the right column of Figure 22.

The computed and preliminarily measured aerodynamic coefficients are shown in Figure 24. The experimental results were filtered using a cut-off frequency of 2.3 Hz, four times the flapping frequency. Although the experimental measurements are still in progress, the computed results lie reasonably between the measured data and the ones obtained at Advanced Subsonics Inc. using a time-stepping vortex-lattice model (VLM) based on a potential flow assumption coupled with separation models.²⁴

As the lift generated during the second half of the flapping cycle cancelled the lift generated during the first half of the cycle, resulting in zero time-averaged lift, the future aircraft will rotate for 90° so that it is vertical and can remain aloft at hovering conditions.²⁵ This indicates that the “lift” – the actual side force, under such conditions – contributes little whereas the thrust plays a dominant role at the hover conditions. The negative value of the drag shown in the figure is indicative of a thrust component, which would vector towards the real lift.

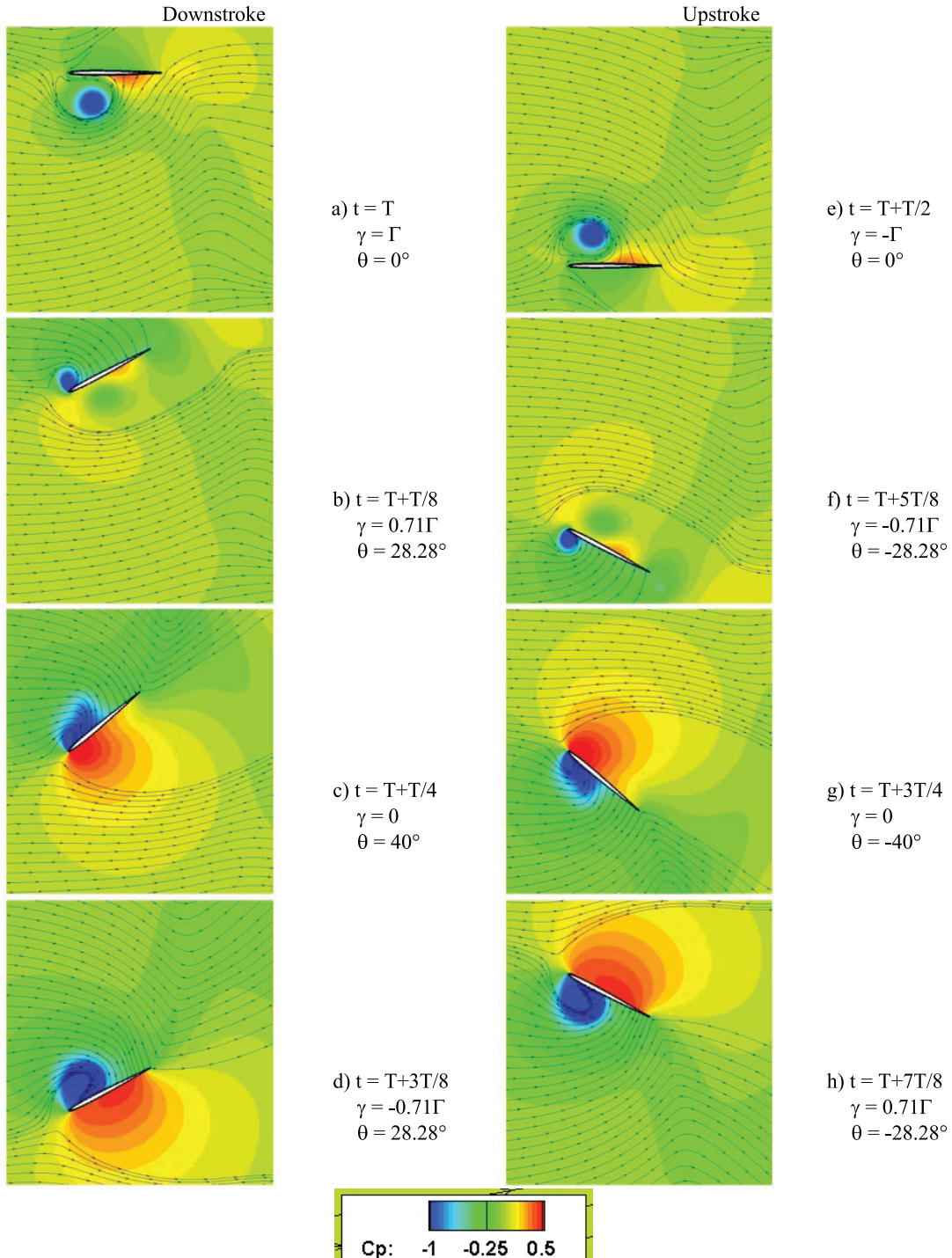


Figure 18. Computed flowfield over the flapping wing at $Re = 19 \times 10^3$, $U_\infty = 0.0635$ m/s; reference cross-section.

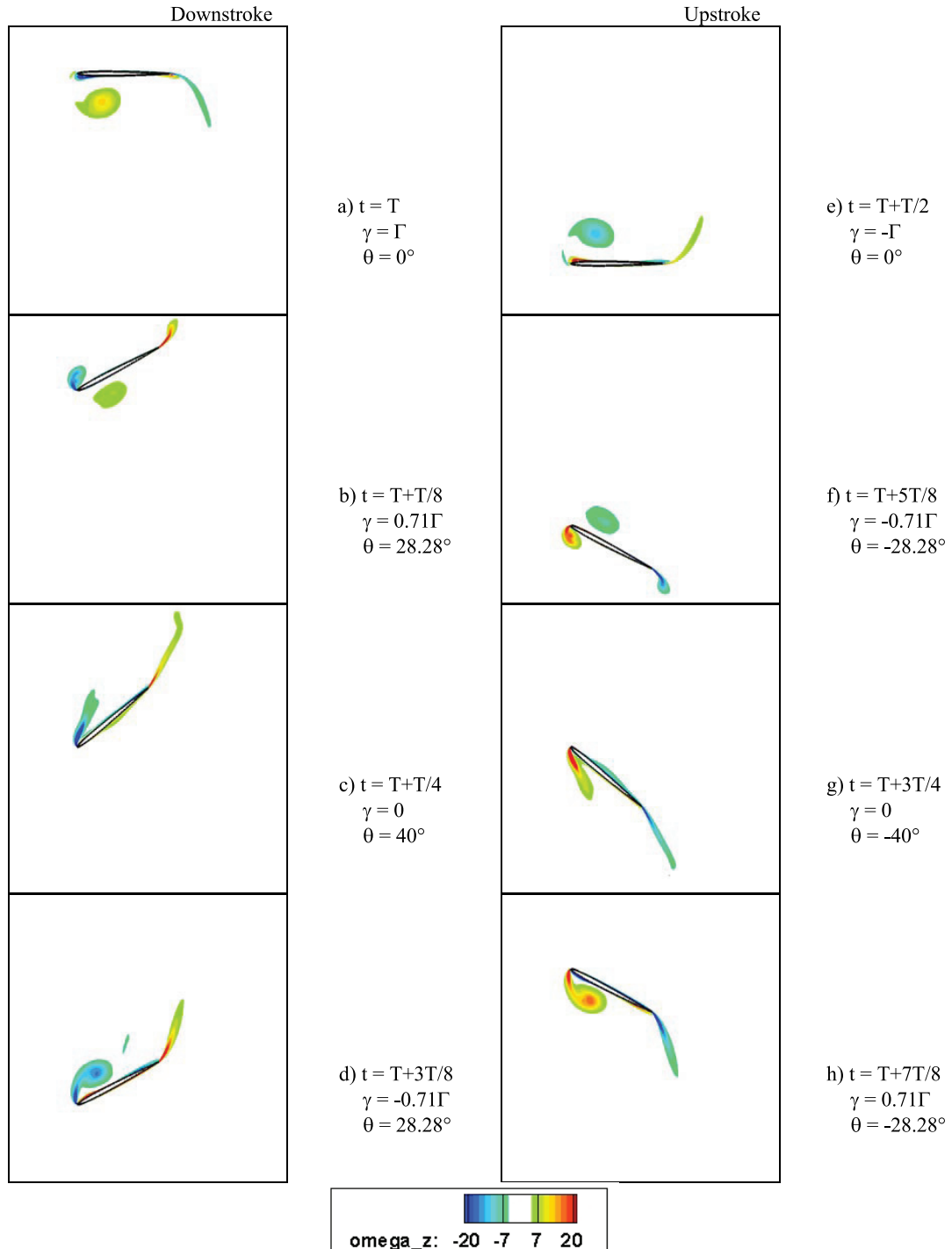


Figure 19. Computed spanwise vorticity distributions over the flapping wing at $Re = 19 \times 10^3$, $U_\infty = 0.0635$ m/s; reference cross-section.

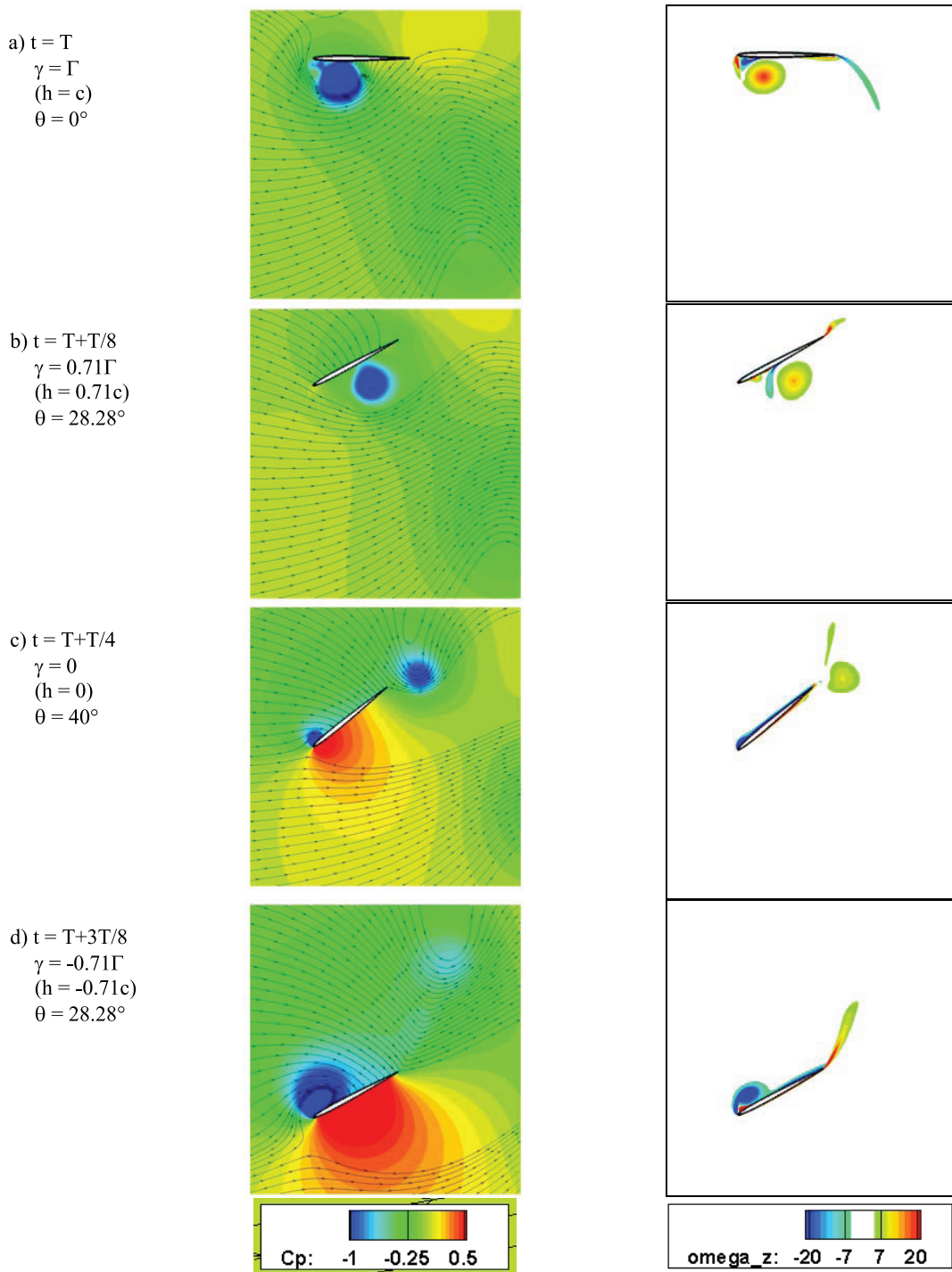


Figure 20. 2D flowfield over the pitching-plunging NACA 0005 airfoil during downstroke at $Re = 15 \times 10^3$, $U_\infty = 0.0635$ m/s.

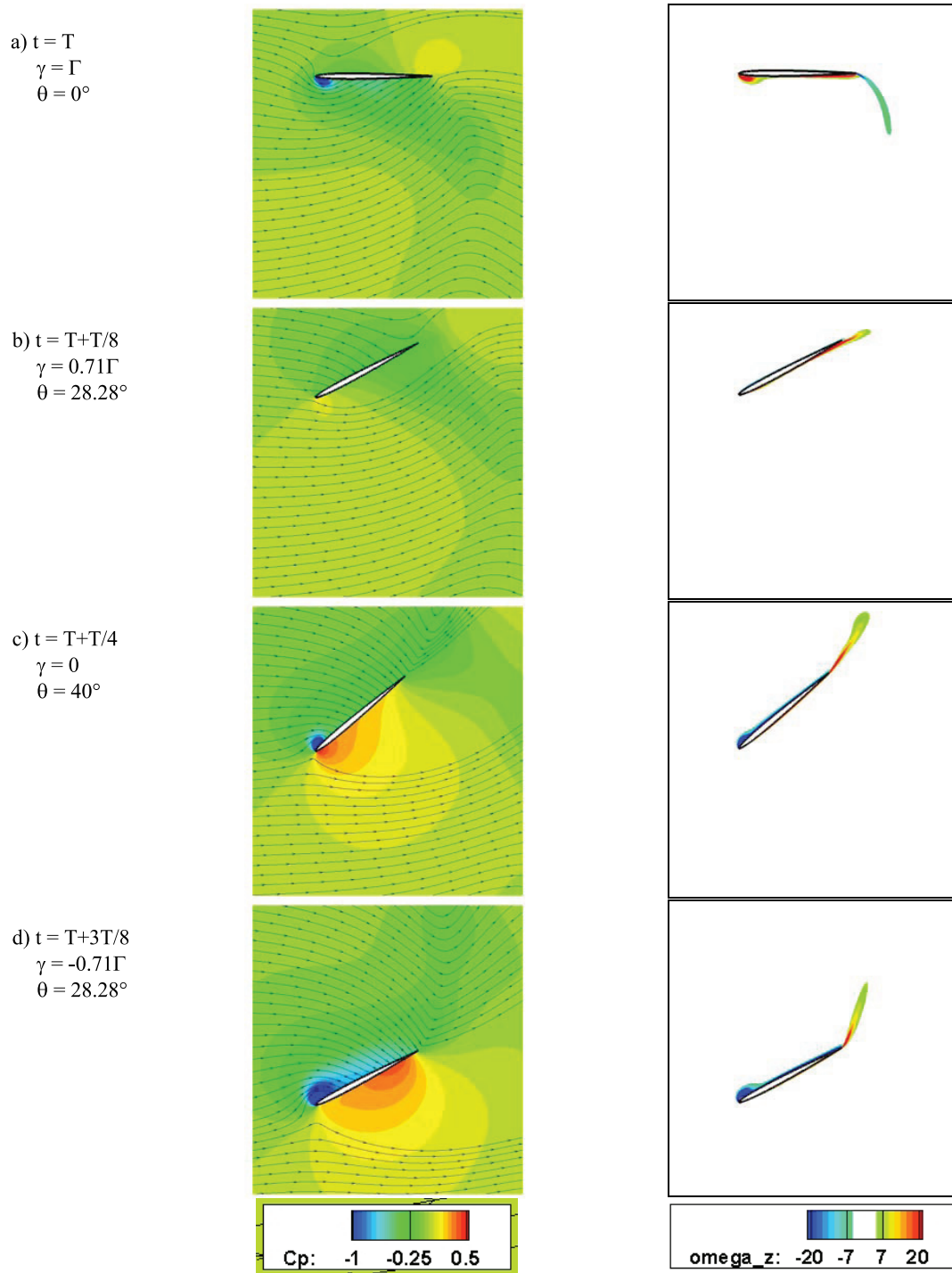


Figure 21. Computed flowfield over the flapping wing during the downstroke at $Re = 19 \times 10^3$, $U_\infty = 0.0635$ m/s; cross-section near the wing root.

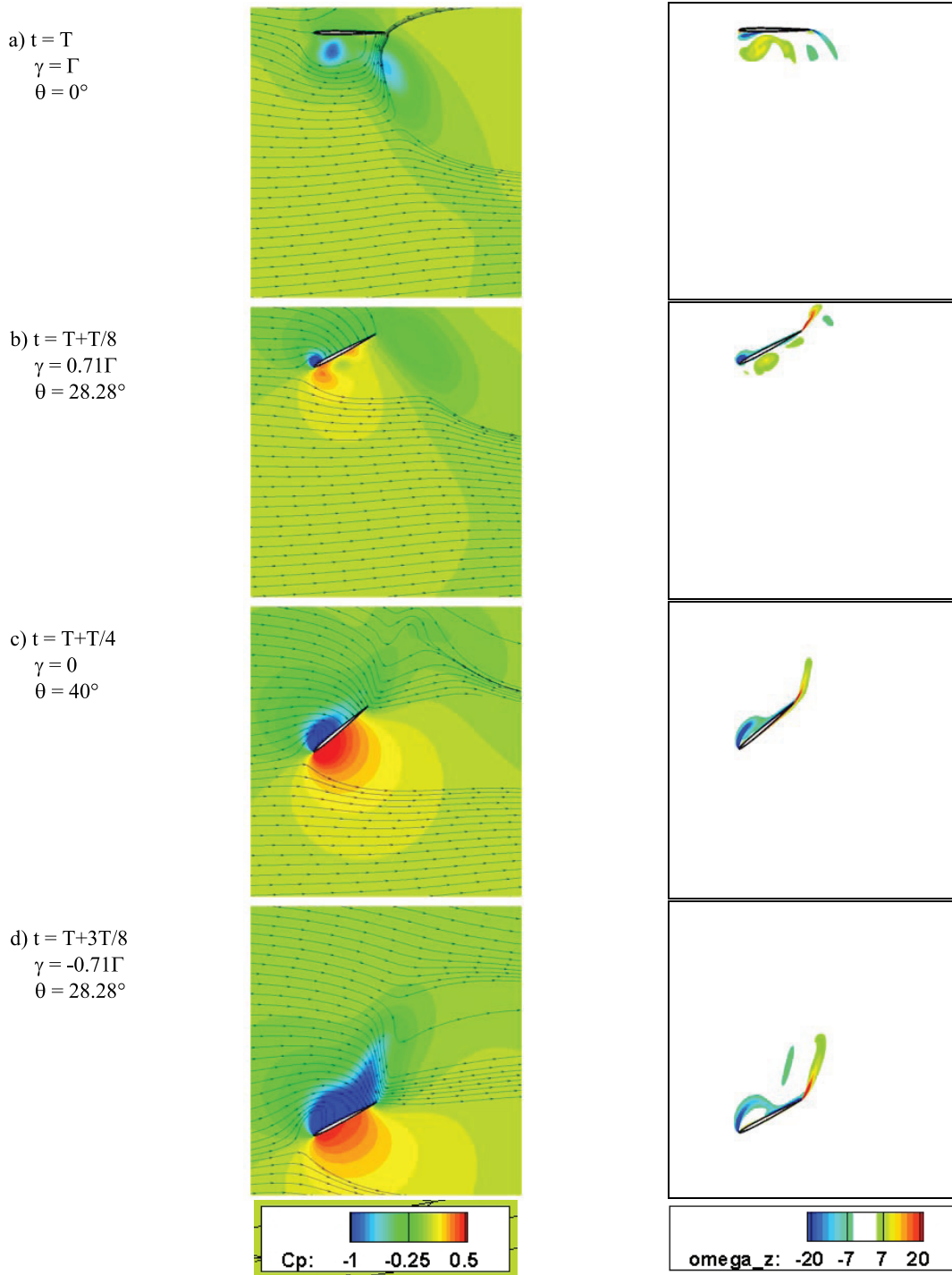


Figure 22. Computed flowfield over the flapping wing during the downstroke at $Re = 19 \times 10^3$, $U_\infty = 0.0635$ m/s; cross-section near the wing tip.

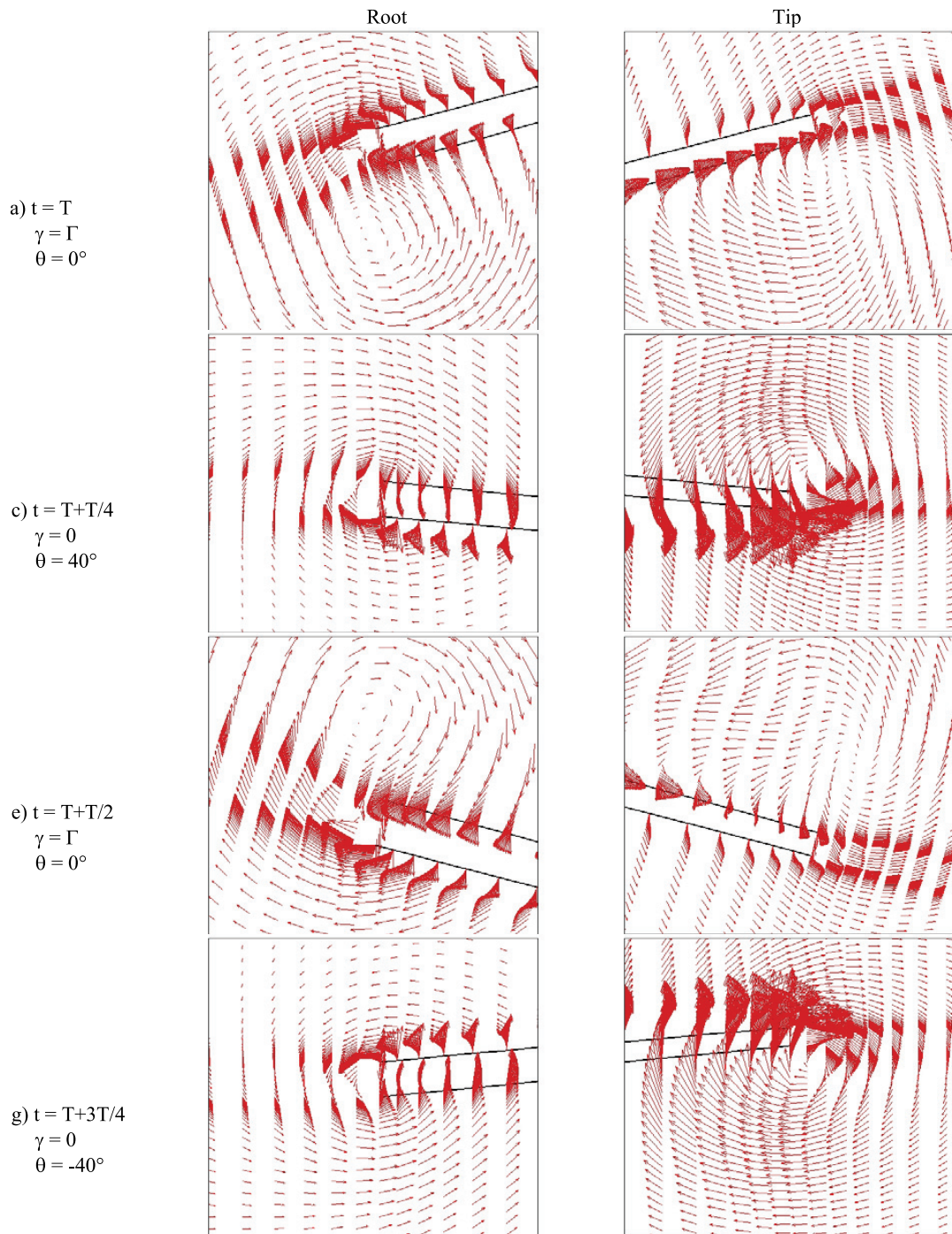


Figure 23. Flowfield around the root and the tip of the flapping wing at $Re = 19 \times 10^3$ (downstream view).

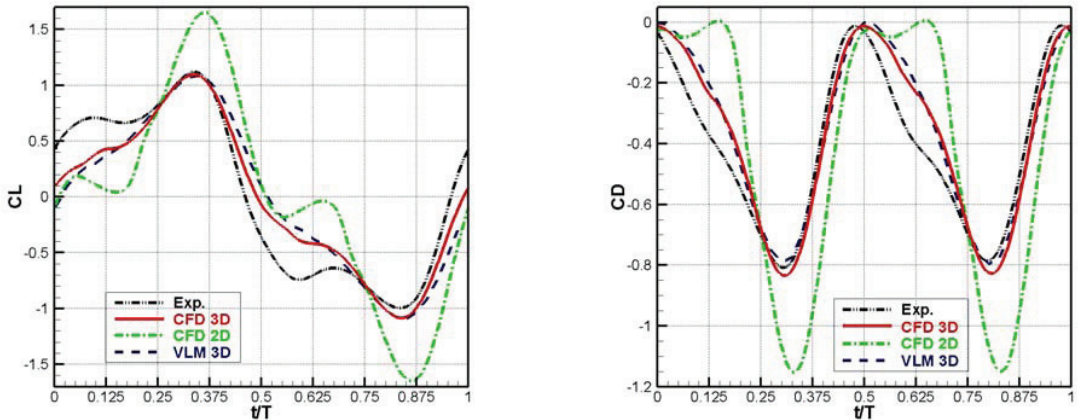


Figure 24. Computed and measured aerodynamic coefficients of the flapping wing at $Re = 19 \times 10^3$, in comparison with the results adopted from Ref. 24 obtained using a vortex-lattice model.

Scrutinizing the measured data closely, one can see that the values of the two peaks of the aerodynamic coefficients deviated. They read 1.12 vs. -1.0 in C_L and -0.809 vs. -0.785 in C_D , respectively. The deviation is believed to be attributed to the effects of the vortex shed in the wake. The leading-edge vortex emerging into the wake during the previous half cycle (cf. Figure 16) affected the flowfield of the next half cycle, promoting a vortex memory effect. This asymmetrical phenomenon in time was observed in the 2D second-order numerical simulations (see Figure 7) while it was smeared in the current 3D first-order CFD calculations. Another sharp discrepancy between the computed and the measured results was observed at around $t/T = 0$. At this time instant, the wing was moved to the maximum flapping angle, with the intensive tip and root vortices as shown in Figure 23a. Although the tip vortex was captured in the current 3D CFD simulations, the vorticity intensity might be inaccurate. On the other hand, the current CFD simulation did not consider tunnel wall effect. The close proximity of the wing tip to the tunnel wall may lead to the suppression of the tip vortex resulting in higher pressure (or lower suction) on the lower surface of the wing. Further investigation is necessary.

For comparison purposes, the 2D CFD results are also plotted in Figure 24. It should be noted that the 2D results were normalized using the generalized velocity of the 3D flapping wing containing the tip velocity. Compared with the 2D results, the drag coefficient of the 3D flapping wing was more sinusoidal. The sinusoidal nature was plausible as the flow was largely three-dimensional and affected by the tip-vortex-like flow. Nevertheless, the 2D calculations clearly over-predicted the force generation. This is a warning sign for engineering design that one cannot simply rely on the 2D results without consideration of the 3D effects of a low-aspect-ratio wing.

6. CONCLUSIONS

Numerical simulations were performed for a symmetrical NACA 0005 airfoil in combined pitching-plunging motions at low Reynolds numbers. The calculations confirmed that the airfoil flapping motion gave rise to regular vortex generation on the upper and lower surfaces. The vortices traversing past the upper and lower surfaces were convected and appeared to dissipate more quickly with a small freestream velocity compared to the condition with zero freestream velocity. At the pure hovering condition where the freestream velocity was zero, both leading-edge and trailing-edge separations were observed on the upper surface during the first half cycle (downwards plunging) of the flapping motion, while the leading-edge separation only occurred on the other surface during the second half cycle. This asymmetry in time of the flowfield led to a time-dependent asymmetry of the aerodynamic performance.

A preliminary investigation of flows past an insect-like wing was also performed. The calculations showed that the flow separation always persisted on the wing surfaces, confirming that insect wing flapping flight may remain in a separated flow pattern. The separated flow was fully three-dimensional, which made convergence of the computations extremely difficult. A tip vortex was also observed, which is believed to interact with the wing body itself or other wings if multi wings are applied. In addition, the 2D calculations of a representative cross-section showed that the 2D computations clearly over-predicted the forces compared with a real low-aspect-ratio 3D wing.

ACKNOWLEDGMENTS

The authors gratefully acknowledge the support of DRDC Valcartier by partially funding this research during the “Flapping wings for nano air vehicles” project under agreement SDA06-153. Sincere thanks are given to the project team members F. Lesage and N. Hamel from DRDC Valcartier, and P. Zdunich from Advanced Subsonics in Montreal, for designing the test cases and for their fruitful discussions.

REFERENCES

- [1] Savage, S. B., Newman, B. G. and Wong, D. T. M., “The Role of Vortices and Unsteady Effects during the Hovering Flight of Dragonflies”, *Journal of Experimental Biology*, 83:59-77, 1979.
- [2] Francis, R. H and Cohen, J., ‘The Flow near a Wing Which Starts Suddenly from Rest and Then Stalls”, *Rep. Memo. Aeronaut. Res. Comm. (Coun.)*, 1561, 1933.
- [3] Weis-Fogh, T., “Quick Estimates of Flight Fitness in Hovering Animals, including Novel Mechanisms for Lift Production”, *Journal of Experimental Biology*, 59:169-230, 1973.
- [4] Ellington, C. P., “The Aerodynamics of Hovering Insect Flight”, *Philosophical Transactions of the Royal Society of London, Ser. B Biological Sciences*, 305(1122):79-113, 1984.
- [5] Mueller, T. J., *Fixed and Flapping Wing Aerodynamics for Micro Air Vehicle Applications*, American Institute of Aeronautics and Astronautics, Inc., Reston, 2001.
- [6] Shyy, W., Lian, Y., Tang, J., Viieru, D., and Liu, H., *Aerodynamics of Low Reynolds Number Flyers*, Cambridge University Press, New York, 2008.
- [7] Liu, H., Ellington, C. P., Kawachi, K., Van Den Berg, C., and Willmott, A. P., “A Computational Fluid Dynamic Study of Hawkmoth Hovering”, *Journal of Experimental Biology*, 201:461-477, 1998.
- [8] Liu, H. and Kawachi, K., “A Numerical Study of Insect Flight”, *Journal of Computational Physics*, 146:124-156, 1998.
- [9] Chorin, A. J., “Numerical Solution of the Navier-Stokes Equations”, *Math. Comput.*, 22:745, 1968.
- [10] Neef, M. F. and Hummel, D., “Euler Solutions for a Finite-Span Flapping Wing”, in Mueller, T. J. (ed.), *Fixed and Flapping Wing Aerodynamics for Micro Air Vehicle Applications*, American Institute of Aeronautics and Astronautics, Inc., Reston, 2001.
- [11] Windte, J., Radespiel, R., and Neef, M., “Aerodynamics Analysis of Flapping Airfoil Propulsion at Low Reynolds Numbers”, in Kroll, N. and Fassbender, J. K. (eds.), *MEGAFLOW – Numerical Flow Simulation for Aircraft Design*, Springer-Verlag, Berlin, 2005.
- [12] Yuan, W. and Khalid, M., “Computation of Unsteady Flows past Aircraft Wings at Low Reynolds Numbers”, *Canadian Aeronautics and Space Journal*, 50(4): 261-271, 2004.
- [13] Yuan, W., Khalid, M., Windte, J., Scholz, U., and Radespiel, R., “Computational and Experimental Investigations of Low-Reynolds-Number Flows past an Airfoil”, *The Aeronautical Journal*, 111(1115):17-29, 2007.
- [14] Yuan, W., Xu, H., Khalid, M., and Radespiel, R., “A Parametric Study of LES on Laminar-turbulent Transitional Flows past an Airfoil”, *International Journal of Fluid Dynamics*, 20(1): 45-54, 2006.
- [15] Yuan, W. and Khalid, M., “Preliminary CFD Studies of Flapping-Wing Aerodynamics”, *Canadian Aeronautics and Space Journal*, 54(3/4):51-63, 2008.
- [16] Patankar, S. V., *Numerical Heat Transfer and Fluid Flow*, Hemisphere Publishing Corporation, Washington, 1980.
- [17] Ferziger, J. H. and Perić, M., *Computational Methods for Fluid Dynamics*, Springer-Verlag, Berlin, 1996.
- [18] Yuan, W. and Schilling, R., “Numerical Simulation of the Draft Tube and Tailwater Flow Interaction”, *Journal of Hydraulic Research*, 40(1):73-81, 2002.
- [19] Demirdžić, I. and Perić, M., “Finite Volume Method for Prediction of Fluid Flow in Arbitrarily Shaped Domains with Moving Boundaries”, *International Journal for Numerical Methods in Fluids*, 10:771-790, 1990.

- [20] Huang, X. and Brown, T., "Preliminary Experiments of a Flapping Wing in Three-Degrees-of-Freedom Motions", *25th International Congress of the Aeronautical Science*, Hamburg, Germany, Sept. 3-8, 2006.
- [21] Dickinson, M. H., Lehmann, F.O., and Sane, S.P., "Wing Rotation and the Aerodynamic Basis of Insect Flight", *Science*, 284:1954-1960, 1999.
- [22] Sane, S.P. and Dickinson, M.H., "The Control of Flight Force by a Flapping Wing: Lift and Drag Production", *Journal of Experimental Biology*, 204:2607-2626, 2001.
- [23] Ruijsink, R., Remes, B., Wagter, C., and Croon, G., "Challenges in the Design of Small Flapping Wing Reconnaissance Aircraft", *RTO-AVT-168 Symposium on Morphing Vehicles*, Evora, Portugal, April 20-23, 2009.
- [24] Zdunich, P., "Development and Application of a 3D Vortex Panel Model with Leading Edge Separation Suitable for Hovering Flapping-Wing Flight", *Technical Report*, Advanced Subsonics Inc., May 2010.
- [25] Lesage, F., Hamel, N., Yuan, W., Khalid, M., and Huang, X., "Aerodynamic Study of a Flapping-Wing NAV using a Combination of Numerical and Experimental Methods", *26th AIAA Applied Aerodynamics Conference*, Hawaii, Aug. 18-21, AIAA 2008-6396, 2009.

